Combining performances of E(m)-corrected LII and absorption for in situ measurements of the volume fraction of 2–4 nm soot particles.

Pascale Desgroux, Nathalie Lamoureux, Alessandro Faccinetto

Journal of Aerosol Science 179 (2024) 106385

Contents lists available at ScienceDirect

Journal of Aerosol Science

journal homepage: www.elsevier.com/locate/jaerosci

Combining performances of E(m)-corrected LII and absorption for in situ measurements of the volume fraction of 2–4 nm soot particles.

Pascale Desgroux *, Nathalie Lamoureux, Alessandro Faccinetto

Univ. Lille, CNRS, UMR 8522 - PC2A - Physicochimie des Processus de Combustion et de l'Atmosphère, F-59000, Lille, France

ARTICLE INFO

Keywords:
2–4 nm soot
Absorption function
Laser induced incandescence
Cavity ring down extinction
Scanning mobility particle sizing
nucleation flame

ABSTRACT

Determining the soot volume fraction (f_v) in combustion environments requires detailed knowledge of the optical properties of the soot particles, and in particular of their absorption function E(m). This study addresses a fundamental lack of information on the optical properties of 2–4 nm soot particles. Recent works based on the modeling of the photoelectron emission yields and UV-vis-NIR-absorption measurements found a sharp decrease of E(m) with the particle size in the vis-NIR spectral region, which is inconsistent with the in situ detection of 2–4 nm particles in the near-infrared region by laser-induced incandescence (LII) or sensitive absorption methods like cavity ring-down extinction (CRDE). The objective of this study is twofold: first, an original method for the determination of E(m) of soot particles, including 2–4 nm particles is proposed. Then, the dynamic of two widespread in situ diagnostics, LII and CRDE, are compared over three orders of magnitude of f_v in atmospheric premixed ethylene/air flames with different flow rates and C/O. The determination of the absolute value of $E(m)$ and of its variation in the flames is derived from an original analysis, which does not require complex LII modeling. This analysis is based on the comparison between the experimental and calculated LII/LII_{max} signals in the low fluence regime, LII_{max} being the plateau value of the fluence curve, which is reached at fluence larger than 1 J/cm^2 for the smallest C/O. E(m) is found to vary between 0.15 at low C/O up to 0.36 for the richest flames. Concerning the comparison of the dynamics of LII and CRDE, an excellent agreement is found above a threshold $(C/O)_{limit}$, while LII exhibits a stronger decrease with C/O below $(C/O)_{limit}$. This discrepancy is attributed to the spectral dependence of E(m) which is negligible above $(C/O)_{limit}$, but increases when C/O decreases below $(C/O)_{limit}$. The particle size distribution function (PSD), measured by scanning mobility particle sizing, reveals monomodal or bimodal PSDs with soot having mobility diameter in the range 2.3–7.5 nm depending on the flame conditions. It is suggested that the particles contained in the first PSD mode, which is dominant in the low C/O range, could be affected by a significant spectral dependence of E(m) in comparison with the second PSD mode.

1. Introduction

Soot formation is a highly complex process that has been the subject of many studies (Appel et al., 2000; Frenklach, 2002; Frenklach

* Corresponding author.
E-mail address: pascale.desgroux@univ-lille.fr (P. Desgroux).

https://doi.org/10.1016/j.jaerosci.2024.106385
Received 18 December 2023; Received in revised form 15 April 2024; Accepted 15 April 2024
Available online 20 April 2024

& Mebel, 2020; Haynes & Wagner, 1981; Thomson, 2023; Wang, 2011). To progress in the understanding of soot formation, several diagnostics were implemented to explore the molecular precursors in the gas phase and the soot particles in the condensed phase all along their growth and oxidation in flames (D'Anna, 2009; Desgroux et al., 2013; Martin et al., 2022; Michelsen, 2017). Primary particle monomers with diameter as small as 2−4 nm (Michelsen et al., 2020), were observed at the onset of the sooting zone (incipient soot particles) or all along the axis of flames stabilized near the sooting threshold such as nucleation flames. The latter soot particles are composed of partially matured soot particles resulting from incipient soot particles (formed at the inception point) having undergone chemical transformations along their residence time in the flame but retaining an almost constant size mix with incipient soot particles formed along the nucleation flame due to the persistent presence of soot precursors (Aubagnac-Karkar et al., 2018; Betrancourt et al., 2022). For convenience, the latter are referred to as "very small soot particles" in the following, while soot particles detected at the onset of the soot profile are referred to as "incipient soot particles". Where it is not necessary to distinguish between them, we refer to them as 2–4 nm soot particles. Essentially two experimental approaches have been developed for the detection of 2-4 nm soot particles. The first approach is based on the online extraction of the particles from the flame, which are subsequently grown into μm-sized droplets that are counted individually. Often, commercial instruments like scanning mobility particle sizers (SMPS) retrofitted to pre-grow particles as small as 1 nm are used (Betrancourt et al., 2017; Camacho et al., 2015; Carbone et al., 2017; Commodo et al., 2015; Hagen et al., 2023; Maricq et al., 2003; Stirn et al., 2009; Tang et al., 2017; Tian et al., 2004; Zhao et al., 2007). The second approach is based on in situ high-sensitivity particle detection using light extinction-based techniques, mainly cavity ring-down extinction (CRDE) (Betrancourt et al., 2019; Desgroux et al., 2017) and laser-induced incandescence (LII) (Betrancourt et al., 2019; Bladh et al., 2015; Desgroux et al., 2017; Johansson et al., 2017). The optical approach requires knowledge of the optical properties of the 2–4 nm particles. The soot absorption coefficient (K_{abs}) is generally expressed as $K_{abs} = 6\pi E(m) f_v/\lambda$ where $E(m)$ is the soot absorption function, m the refractive index, λ the wavelength and f_v the soot volume fraction. Although the optical properties of soot particles can be obtained by combining extinction and gravimetry measurements provided that the collected mass is sufficient (Choi et al., 1995; Williams et al., 2007), the $E(m)$ of incipient soot and of very small soot particles remains affected by a large uncertainty to date since in situ absorption-based techniques only give access to the relative variation of $E(m)$ (i.e., with respect to a given soot). For instance, $E(m)$ strongly decreases as a function of the wavelength, and this decrease is more pronounced for incipient soot particles found at low height above the burner (HAB) of premixed flames (Migliorini et al., 2011; Simonsson et al., 2015; Yon et al., 2011). However, it is not possible to determine by absorption the variation of $E(m)$ of different soot particles (at different HABs, for example) unless the f_v or the soot mass are otherwise known. An alternative to access the absolute value of $E(m)$ that does not rely on a priori knowledge of the f_v involves the modeling of the thermal response of the particles under the laser excitation as used in LII. This modeling is based on the unsteady energy and mass conservation equations of a primary particle. Measuring the temperature of laser-heated soot particles and assuming their size, the $E(m)$ of incipient particles or very small soot particles can be determined by matching the simulated and experimental temperature as a function of the fluence (Bejaoui et al., 2015; Betrancourt et al., 2017; Eremin et al., 2020; Lemaire & Menanteau, 2023; Maffi et al., 2011; Olofsson et al., 2015; Snelling et al., 2004).

Currently, data on the optical properties of incipient soot particles is scarce. The absorption $E(m)$ and scattering $F(m)$ functions of thermophoretically sampled incipient soot particles of around 3 nm diameter were obtained from the modeling of photoelectron emission yields and absorption spectra (Wan et al., 2021) based on quantum confinement (C. Liu et al., 2019), or from UV–vis–NIR absorption measurements (Minutolo et al., 2023) combined to previously reported in situ absorption and scattering measurements at 266 nm (Cecere et al., 2002). These investigations found a strong decrease of $E(m)$ in the vis-NIR region, which is consistent with the visible-transparent particle appellation previously reported, e.g. in (D'Anna et al., 1994). In particular, the predicted imaginary part of the refractive index (k) shows a significant dependence on the particle size (from 5 nm to 32 nm) and wavelength (185–1400 nm). While the decrease of k with size is moderate at 266 nm (from 0.95 at 32 nm down to 0.73 at 5 nm), it varies from 0.42 down to 0.02 in the same size range at 1064 nm. These results also apply to $E(m)$, which scales linearly with k (Wan et al., 2021). In conclusion, these investigations indicate that the absorption efficiency of incipient soot particles is extremely low in the visible and near-IR.

And yet, several in situ experiments report the detection of 2–4 nm soot particles either at the onset of the soot flame zone or along very low sooting flames such as nucleation flames (Betrancourt et al., 2019; Bladh et al., 2015; Do et al., 2022; Johansson et al., 2017). Nucleation flames are peculiar premixed 1D flames that provide very small soot particles having almost constant diameter that does not evolve with HAB. Particularly, in (Betrancourt et al., 2017), it was found from time-resolved LII (TIRE-LII) modeling that the incipient soot particles found at the onset of a slightly sooting flame and the very small soot particles found all along the axis of a n-butane nucleation flame had the same particle size distribution and similar thermal and optical properties, leading to $E(m) = 0.26$ at 1064 nm for this entire set of 2–4 nm soot particles. The interpretation of kinetics modeling for this lack of particle growth is based on the competing and balanced particle growth and consumption mechanisms (Aubagnac-Karkar et al., 2018; Betrancourt et al., 2022; Desgroux et al., 2017; Kholghy et al., 2018). To identify and measure very small soot particles, researchers rely on measurements of the size distribution by SMPS or microscopic analysis (Betrancourt et al., 2017; Carbone et al., 2017; Moallemi et al., 2018; Schenk et al., 2015), or by extracting the primary particle diameter from TIRE-LII modeling (Bladh et al., 2011; F. Liu et al., 2006). These measurements reveal particles between 1.5 and 4.0 nm. In addition, some of these works provide laser-induced emission spectra of 2–4 nm soot particles behaving like a blackbody (Betrancourt et al., 2017; Mouton et al., 2013). The derived temperature of laser-heated soot particles at the soot inception point of a slightly sooting flame and all along a nucleation flame were shown to be similar, confirming that the optical properties of incipient soot and very small soot particles are very close in these premixed n-butane atmospheric flames (Betrancourt et al., 2017). By studying the behavior of the LII fluence curves (which represent the response of the LII signal to the laser fluence) in atmospheric butane flames including a nucleation flame, Betrancourt et al. (Betrancourt et al., 2019) estimated that $E(m)$ of incipient soot and very small soot particles measured at 1064 nm was 1.6 times lower than mature soot. Using a similar approach, Olofsson et al. (Olofsson et al., 2015) determined that $E(m)$ evolves from around 0.20 at the onset of ethylene premixed sooting flames

up to 0.34 in the burnt gases. In the context of nucleation flames, in situ LII/CRDE measurements combined with species analysis from gas chromatography after probe sampling revealed concordant results and were satisfactorily modeled (Aubagnac-Karkar et al., 2018; Betrancourt et al., 2022; Desgroux et al., 2017; Kholghy et al., 2018), giving confidence in the reliability of the measured f_v of 2–4 nm soot particles.

The research discussed above shows that in situ detection of 2–4 nm soot particles is possible. The absorption wavelength for detecting 2–4 nm soot particles has to be greater than 700 nm to avoid the absorption by polycyclic aromatic hydrocarbons (PAHs) or soot precursors at lower wavelengths (Migliorini et al., 2011; Schoemaecker Moreau et al., 2004; Zerbs et al., 2009), which would lead to an overestimation of the absorption on the one hand, and of the LII signal on the other, to which laser induced fluorescence from PAHs is added. In addition, the detection of 2–4 nm soot particles requires a specific experimental setup to decrease the detection threshold of the LII. For example, if $E(m)$ is assumed to be invariant with soot maturity, the signal of a 3 nm particle is roughly 300 times weaker than a 20 nm particle.

As previously mentioned, LII and CRDE are very interesting diagnostics for measuring in situ the f_v of flames with very low detection limit, and are therefore valuable tools for studying the early steps of soot formation. In general, f_v profiles are deduced from LII profiles, which have high spatial resolution, and calibrated at a certain flame HAB by single-path extinction or CRDE. The LII signal profile is then transformed into an absolute f_v profile, with the implicit assumption that the soot optical properties do not vary along the profile.

In this work, we compare the dynamic of LII and CRDE over a wide range of f_v, which was never explored before. To do this, measurements were performed in the burnt gases (HAB = 16 mm) of the flames and only the C/O parameter was modified. A variation of f_v of around three orders of magnitude (from a few ppt to a few ppb) was achieved by investigating a wide range of atmospheric ethylene/air flames, including nucleation flames, stabilized on a porous burner with different flow rates and equivalence ratios. The size distribution of probe-sampled soot particles was determined by SMPS. CRDE and LII measurements were performed at 1064 nm excitation wavelength. While the two techniques have the same dynamics for the higher f_v, an increasingly large discrepancy was observed for low f_v and very small soot particle size, as found for instance in nucleation flames. The blackbody assumption used for the determination of the temperature of the laser-heated soot particles is found to be a possible cause of this discrepancy, perhaps associated with the shape of the size distribution. This study on the dynamic of LII and CRDE takes into account the variation of $E(m)$ with C/O, determined from a methodology inspired by Betrancourt et al. (2019). The initial methodology, based on monitoring the evolution of the LII fluence curves with C/O, is completed here by an original theoretical approach which allows the determination of the absolute value of $E(m)$. We also present some f_v profiles obtained in nucleation flames and in a slightly sooting flame taken from the literature encompassing both incipient soot and mature soot. Finally, the f_v detection threshold of LII and CRDE is determined.

2. Experiment

2.1. Choice of flames based on the literature and objectives of this work

The flames were stabilized on a 6 cm-diameter bronze porous Holthuis burner at atmospheric pressure mounted on a vertical translation stage for the accurate determination of the HAB. All experiments were performed at ambient temperature and pressure. The burner was surrounded by a co-annular N_2 flow to prevent the formation of a diffusion flame between the unburnt fuel and the surrounding air. The shielding co-flow of nitrogen was 20 L min^{-1} (273 K, 1.013 × 10^5 Pa). A stainless steel disk (60 mm diameter, 30 mm thick) was placed 21 mm above the burner surface. The disk was perforated at its center for introducing axially the sampling probe used for SMPS measurements. A water-cooling circuit kept the porous of the burner at a temperature of 323 K during all experiments.

In total, 24 premixed ethylene/air flames were investigated. Synthetic air (80% N_2, 20% O_2) was used. The purity of ethylene was >99.95%. Two sets of flames were investigated: F10 and F17 had a total flow rate of 10 L min^{-1} and 17 L min^{-1} respectively. The cold gas velocity was 5.9 cm s^{-1} and 10.0 cm s^{-1}, respectively. The C/O of the flames was selected to cover a range of measurable signals attributed to soot particles from the minimum C/O to a larger ratio offering a variation of f_v of around three orders of magnitude. The C/O ranged from 0.57 to 0.70 in F10 and from 0.59 to 0.66 in F17. f_v was measured at constant HAB = 16 mm. Only a few f_v profiles along HAB were measured.

In this work, the results obtained for the studied flames are discussed in relation to the results previously obtained in the literature and briefly reviewed in this section:

(a) (Bladh et al., 2015) identified F10 with C/O = 0.59 (F10-0.59) as a nucleation flame. Incipient soot particles were detected by LII. The LII decay times were short (~5 ns) and did not exhibit any increase with HAB by contrast to F10-0.62 and F10-0.67. The denomination “nucleation flame”, linked to the constancy and short decay time was used with several premixed flames, at low or atmospheric pressure, with different fuels (Betrancourt et al., 2017; Bladh et al., 2015; Desgroux et al., 2017; Do et al., 2022). From TIRE-LII modeling, the particle diameter was estimated to 1.0–1.5 nm in F10-0.59 (Bladh et al., 2015). The authors confirmed the important dependence of the fluence curves, which represent the response of the LII signal to the laser fluence, as a function of the equivalence ratio φ. The lower φ, the higher the energy threshold to which the LII signal starts to increase. By contrast to what was long observed for mature soot, the LII fluence curve in nucleation flame approaches a plateau only at fluences higher than 1.2 J/cm^2 (Bladh et al., 2015). This was attributed to a lower absorption soot function $E(m)$ for the incipient soot particles produced in the nucleation flames.

(b) The spectral dependence of $E(m)$ against HAB, between 450 nm and 900 nm, was studied in F10 with C/O = 0.7 (F10-0.7) by line-of-sight attenuation by Migliorini et al. (2011). Soot was assumed to be the only constituent in the optical path absorbing

light, meaning that the $E(m)$ inferred from the extinction coefficient implicitly contains the contribution of large PAHs in the visible spectral range. A substantial decrease of $E(m)$ (in relative value) was found with wavelength, due in part to the contribution of large PAHs in the visible range. This decrease was found much more pronounced for incipient soot at the lowest HABs. $E(m)$ was found to be nearly constant above 700 nm.

(c) f_v profiles and the spectral dependence of $E(m)$ with HAB was studied in F10-0.7 by single-pass absorption from 405 nm to 1064 nm by Simonsson et al. (2015). Extinction as low as 10^{-4} could be measured, corresponding to f_v of 0.1–0.3 ppb. As for the above-mentioned study, an important dependence of K_{abs} was found with the wavelength with a more pronounced trend at low HAB. The dispersion coefficient α defined as $K_{abs} \propto {}^{1}/_{\lambda^{\alpha}}$ was evaluated between 685 and 1064 nm to avoid influence of PAH absorption. α was found to sharply decrease from 4 at HAB = 5 mm down to 1 at high HAB. This means that incipient soot at low HAB had a much stronger wavelength dependence than mature soot found at high HAB where α approaches 1 as expected for mature soot (Forestieri et al., 2018). In the studies of Migliorini et al. (2011) and Simonsson et al. (2015), the absorption techniques only gave access to the relative spectral variation of $E(m)$ (for a given soot) but it was not possible to determine the variation of $E(m)$ for different soot particles (different HABs, for example).

(d) Sgro et al. (2009) compared size distributions of probe-sampled particles detected with a differential mobility analyzer (DMA), by atomic force microscopy (AFM) after thermophoretic sampling, and by in situ single-pass absorption measurements in F17 with C/O ranging from 0.50 (F17-0.50) to 0.77 (F17-0.77). The authors detected particle sizes between 1 and 5 nm from C/O = 0.56. They defined the soot formation threshold as the value of C/O where visible absorption and LII were detected. For their flame conditions, this threshold was found equal to C/O = 0.70. They attributed particles detected below this threshold by absorption, DMA and AFM to nanoparticles of organic carbon (NOC).

(e) (Commodo et al., 2015) investigated soot inception in F17-0.67. They reported a progressive modification of the particle size distributions obtained by SMPS, from a unimodal distribution centered around 2 nm at low HAB to a bimodal distribution at high HAB. As mentioned in the introduction, Minutolo et al. (2023) determined the optical properties of incipient soot probed at low HAB in this flame and found a decrease of $E(m)$ in the vis-NIR region, consistent with the visible-transparent particle appellation previously reported in (D'Anna et al., 1994).

(f) (Bocchicchio et al., 2022) investigated several F17 flames from C/O = 0.61 to 0.72 at different HAB. Soot particles were thermophoretically sampled on quartz fiber filters for thermo-optical-transmission and Raman spectroscopy analyses. The authors reported an important change of the elemental and organic carbon content depending on the maturity of the soot samples and found a mass absorption coefficient (MAC) at 678 nm ranging from 2 to 6 $m^2\ g^{-1}$ depending on the organic content. Provided the soot density ρ is known, the values of $E(m)$ can be calculated from the equation: $MAC = 6\pi E(m)/\lambda\rho$ (F. Liu et al., 2020).

Most important observations in the above mentioned works are summarized in Table 1.

2.2. Laser-based techniques

The laser used for the LII and CRDE experiments was a Nd:YAG laser (Quantel QSMART 850) operating at 1064 nm with a Gaussian beam of 9 mm diameter and a repetition rate of 10 Hz. The laser beam was aligned parallel to the burner surface and shaped to suit the used technique (LII or CRDE) as detailed in (Betrancourt et al., 2019). f_v was measured by two techniques: (1) The LII allows to measure f_v on the burner axis at a selected HAB (16 mm in this work). LII measurements were converted to absolute f_v by a calibration procedure

Table 1
Non-exhaustive list of investigations in flames F10 and F17. (a): F10 flames, (b) F17 flames.

	C/O	Method	Size (diameter d)	Observation
Bladh 2015 (a)	0.59, 0.62, 0.67	Tire-LII λ_{laser} = 1064 nm	d = 1–1.5 nm in C/O = 0.59	Nucleation flame C/O = 0.59 Shift of fluence curves with C/O LII plateau above 1.2 J/cm^2
Migliorini 2011 (a)	0.70	Line-of-sight attenuation; 450−900 nm, TEM	Small soot aggregates	Relative spectral variation of E(m) much more important for incipient soot
Simonsson 2015 (a)	0.70	Line-of-sight attenuation; 405−1064 nm		Relative spectral variation of E(m) much more important for incipient soot. α varies from 4 (low HAB) to 1 (high HAB)
Sgro 2009 (b)	0.50–0.72	SMPS, AFM, single-pass absorption	d from 1 to 5 nm from C/O = 0.56	Soot formation threshold defined at C/O = 0.70. Below this C/O, particles detected by SMPS defined as NOC
Commodo 2015 (b)	0.67	SMPS	From a monomodal (2 nm) PSD at low HAB to a bimodal at high HAB	
Minutolo 2023 (b)	0.67	UV–vis–NIR ex situ absorption,in situ absorption/scattering at 266 nm	d = 2.2 nm at 8 mm. SMPS	E(m) varies from 0.52 at 200 nm to 0.02 at 1064 nm at 8 mm
Bocchicchio 2022 (b)	0.61–0.72	Thermo-optical-transmission + Raman (probe sampled particles), SMPS	2 nm at 15 mm (C/O = 0.61), 3.2 nm at 6 mm and 11.5 nm at 12 mm (C/O = 0.72)	MAC at 678 nm ranges from 2 to 6 $m^2\ g^{-1}$ depending on the organic content

based on CRDE. CRDE is a line-of-sight technique that allows to measure the extinction coefficient K_{ext} with excellent sensibility. From this measurement and neglecting the scattering ($K_{ext} \approx K_{abs}$), the absolute f_v, averaged over the flame diameter l, was simply obtained by $f_v = \frac{\lambda}{6\pi E(m)} K_{abs}\, l$. This last equation considers that the soot is uniformly distributed along the flame diameter, an assumption discussed in section 2.2.2. f_v was measured by LII and CRDE in all flames at HAB = 16 mm.

2.2.1. LII measurements

The LII setup was optimized to maximize the signal-to-noise ratio for the detection of very small incandescent soot particles. The setup is very similar to (Betrancourt et al., 2017). To do so, we first took advantage of the 1D-characteristics of the premixed flame at a given HAB to expand the collection volume in a plane parallel to the burner surface as shown in (Betrancourt et al., 2017, 2019). The volume (located on the flame centerline) was selected from a top-hat fluence distribution profile issued from the transformation of the incident Gaussian laser beam as follows: first, the laser beam was expanded in a horizontal plane using two cylindrical lenses ($f_1 = -40$ mm, $f_2 = 200$ mm). A rectangular slit (0.48 mm vertical axis, 7.2 mm horizontal axis) on the beam path was relay imaged on the burner axis by means of a spherical lens ($f_3 = 300$ mm). The homogeneity of the top-hat profile was monitored with a beam profiler camera (Gentec Beamage). The top-hat fluence distribution ensured that all the particles contained in the collection volume were heated with nearly the same laser fluence, which was varied between 0 and 1.4 J/cm^2 using an optical attenuator. The high value of the laser fluence was necessary to extract accurate data on the absorption function of the smallest particles as explained in section 3.2.1. The fluence was determined by measuring the transmitted laser energy after the flame using a power meter and considering the top-hat fluence distribution. Fluence uncertainty is estimated at ± 10 %.

The LII emission issued from the collection volume was detected by a photomultiplier tube (PMT Hamamatsu H10721-20), having a risetime of 0.57 ns, equipped with an interference filter centered at 532 nm. The collection volume was selected by imaging the horizontal slit placed in front of the PMT into the top-hat laser beam with two achromatic lenses resulting in a volume of 19 mm^3 (Betrancourt et al., 2017).

Additionally, a monochromator (ARC SpectraPro-275, 1200 grooves/mm, 500-nm blazed grating, scan rate = 30 nm/mn) equipped with the same PMT as for LII, was used to collect laser-induced emission spectra allowing to determine the effective temperature of the laser-heated soot particles from blackbody radiation fitting for several flame setpoints.

For all measurements, to determine f_v or the temperature, the LII signal was measured at its temporal peak and recorded by an oscilloscope (LECROY 9354, 8-bit vertical resolution, 500 MHz bandwidth, 1 GS/s sampling rate) triggered by a photodiode (Hamamatsu S1722-02) placed after the burner. Some of the investigated flames exhibited a “nucleation flame” behavior, meaning that the particle size was very small and did not show a measurable growth along the flame. From the experimental point of view, this was easily checked by monitoring the time-resolved LII traces along the flames and by controlling the constancy of the (short) decay-time with HAB (see Supplementary Materials SM1)

2.2.2. CRDE measurements

CRDE is a very sensitive technique well suited for measuring soot extinction (Bouvier et al., 2007; Desgroux et al., 2008; Mercier & Desgroux, 2009; Vander Wal & Ticich, 1999). Again, the setup is very similar to (Betrancourt et al., 2019). In this work extinction as low as 4×10^{-7} was measured, corresponding to f_v of a few ppt (10^{-12}). The CRDE principle consists in introducing a laser beam in a resonant optical cavity and to follow the evolution of the transmitted light as a function of time. The CRDE setup is detailed in (Betrancourt et al., 2019). The sooting flame was placed at the center of the optical cavity. The laser beam was shaped to match the TEM_{00} transverse mode of the cavity. The CRDE cavity consisted of two identical 25 mm diameter plano-concave mirrors (radius of curvature: 25 cm, separated by d = 40 cm, coated to achieve a high reflectivity of R = 99.96% at 1064 nm). The beam waist diameter was estimated to be around 300 μm and nearly constant along the flame diameter, resulting in an absorbing volume of 4.2 mm^3. A photodiode (FGA-InGaAs-10 Thorlab) collected the light transmitted by the second mirror. The signal was recorded by the same oscilloscope as for LII. The experimentally measured signal was exponentially fitted to extract the pulse decay time τ using a fast exponential fitting algorithm for real-time instrumentation with Labview 2020 (Halmer et al., 2004). In non-sooting flames, the losses of light transmission are due to the mirrors and to potential gaseous species absorption. The decay time was found unchanged in a cavity with ambient air or in the cavity containing a soot-free premixed flame at an equivalence ratio of 1.59 (C/O = 0.53), indicating that the contribution of light attenuation by flame gaseous species at 1064 nm is negligible. Under these conditions, the pulse decay time τ_0 of the empty cavity is given by Eq. (1):

$$\tau_0 = \frac{d}{c}\,\frac{1}{(1-R)} \tag{1}$$

In the presence of soot, the pulse decay time τ_{soot} is reduced, due to the additional losses (Eq. (2)):

$$\tau_{soot} = \frac{d}{c}\,\frac{1}{(1-R) + \int_l K_{ext,\lambda}\, dx} = \frac{d}{c} L^{-1} \tag{2}$$

where L is the total loss per pass in the cavity, d the length of the cavity, c the speed of light in vacuum, R the reflection coefficient of the mirrors, l the flame diameter and $K_{ext,\lambda}$ the extinction coefficient of soot at 1064 nm. The 1D-feature of the flame was controlled by collecting the LII signal at right angle to the laser axis at HAB = 16 mm and by translating the burner along one diameter. The obtained radial LII profile was representative of the radial distribution of f_v at this HAB. Contrary to what has been observed in atmospheric

butane/O_2/N_2 (Betrancourt et al., 2019) and ethylene/air flames (Migliorini et al., 2008), the soot distribution in the flames studied was found to be almost flat over 75% of the central part of the flame, decreasing slightly to the edges of the flame (see Supplemental Materials SM2). In the next, we have considered a mean soot extinction coefficient $\overline{K_{ext,\lambda}}$ across the flame diameter l_s determined at 1/e of the normalized LII profile: $\int_l K_{ext,\lambda}\, dx = \overline{K_{ext,\lambda}} l_s$, similarly as in (Betrancourt et al., 2019). By rearranging the above expressions of τ_0 and τ_{soot}:

$$\overline{K_{ext,\lambda}} l_s = \frac{d}{c}\left(\frac{1}{\tau_{soot}} - \frac{1}{\tau_0}\right) \tag{3}$$

In the flames considered in this study, the soot particles are much smaller than the laser wavelength of 1064 nm (see section 3.1). Therefore, the light extinction is dominated by absorption and the contribution of scattering can be confidently neglected. Therefore:

$$\overline{K_{ext,\lambda}} = \overline{K_{abs,\lambda}} = \frac{6\pi E(m,\lambda)\overline{f_v}}{\lambda} = \frac{d}{c l_s}\left(\frac{1}{\tau_{soot}} - \frac{1}{\tau_0}\right) \tag{4}$$

from which the mean soot volume fraction $\overline{f_v}$ across the flame diameter (noted f_v in the next) is obtained.

2.3. SMPS

The particle size distributions (PSDs) were measured online using a nano-SMPS (TSI Inc.) coupled to a sampling system based on dilutive microprobe extraction.

The nano-SMPS system included a soft X-ray neutralizer (TSI 3088), a differential mobility analyzer (TSI DMA 3086) controlled by an electrostatic classifier (TSI 3082), and a nano-enhancer (TSI 3757) coupled to a condensation particle counter (TSI CPC 3570). To minimize diffusion losses, high sampling flow (2.50 L min^{-1}) was used. With this configuration, the SMPS could detect particles with electrical mobility diameter in the 1–30 nm range.

Detailed schemes of the probe and sampling system (Irimiea et al., 2018) and of the nano-SMPS setup (Do et al., 2022) are provided elsewhere. The only major change with respect to (Do et al., 2022) was the removal of the buffer volume. The microprobe used in this work, made of two co-annular quartz tubes and ending with a long thin tip with a 160 μm orifice, was inserted vertically into the flame throughout the burner stabilization plate. Nitrogen (5.00 L min^{-1}) was used as dilution gas.

Post-sampling coagulation was ruled out for the low C/O flames by verifying that the normalized PSDs were independent from the dilution ratio. However, to be able to compare the PSD of different flames, rather than adjusting the dilution ratio for each flame, the same dilution ratio was used in all experiments. Therefore, the PSDs of the high C/O flames are likely affected to some degree by post-sampling coagulation. The PSDs shown below are the raw output of the nano-SMPS. The diffusion losses in the sampling line were considered to be the same for all investigated flames and thus neglected in the comparative study. The flame temperature correction depends on the ratio between the temperature of the dilution gas and the flame temperature at the sampling point, which is also neglected in the comparative study. The dilution ratio was estimated by fluid mechanics simulations to be in the 500–1000 range, but not directly measured.

3. Results

3.1. SMPS

The PSDs in premixed ethylene flames stabilized on a porous burner were measured in numerous works by SMPS. Most works reported the evolution of the PSD as a function of HAB in relatively rich flames. In a C/O range between 0.67 and 0.70 (Carbone et al., 2017; Commodo et al., 2015; Maricq et al., 2003; Stirn et al., 2009), it was shown that at low HAB, the PSD is contained within a single

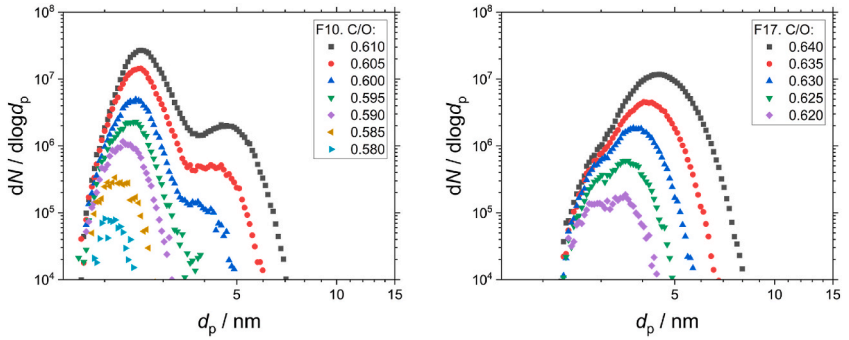

Fig. 1. PSDs of all investigated F10 (left panel) and F17 (right panel) at HAB = 16 mm (160 μm probe orifice, 5.00 L min^{-1} nitrogen dilution flow, 6 mbar differential pressure). The figures show the raw SMPS output, no corrections are applied.

mode centered on a diameter of a few nm, which gradually evolves with HAB toward a bimodal size distribution. Stirn et al. (2009) reported on the evolution of the PSD in a C/O range between 0.60 and 0.73 for a fixed HAB = 12 mm. At low C/O, they observed a single mode, centered around 3–4 nm, attributed to soot precursors. This single mode appeared slightly below the sooting threshold, determined in (Haynes & Wagner, 1981) at C/O = 0.60 based on the onset of (yellow) soot luminosity. As the C/O increases, the first mode persists but a second mode, attributed to soot, appears and increases in number and particle size.

We focused here on the PSDs of the lowest C/O. Fig. 1 reports the PSDs obtained at 16 mm HAB in F10 and F17. The experimental conditions were selected to give access to all C/O across the sooting threshold by using the same dilution flow and flame-probe differential pressure, resulting in the same dilution ratio, that are specifically chosen to allow the direct comparison of the PSDs of different flames while avoiding saturation of the CPC at high C/O. F10 shows a progressive change in the PSD: at low C/O a single mode is detected, while a second mode appears at higher C/O. Single mode PSDs in the burnt gases are typically found in nucleation flames. Here, incipient soot particles formed along the nucleation flame due to the persistent presence of soot precursors (Aubagnac-Karkar et al., 2018; Betrancourt et al., 2022) mix with partially matured soot particles resulting from incipient soot particles (formed at the soot inception point), having undergone chemical transformations along their residence time in the flame but retaining an almost constant size. The higher the C/O, the more shifted to high diameter the position of the second mode, ranging from 4 to 5 nm. The position of the first mode is always lower than 2.8 nm. In contrast, F17 show a much more pronounced second mode from C/O = 0.62, although the first mode is still apparent starting at 2.3 nm regardless of the C/O. The position of the second mode ranges from 4.0 to 7.5 nm.

Once stable flame and sampling conditions were reached (around 2 h wait before beginning any series of measurements), the uncertainty associated to the SMPS measurements was estimated from the standard deviation of five consecutive scans. Typical standard deviations are <15% for $dN/d\log d_p \geq 5 \times 10^5$, and <40% for $dN/d\log d_p < 5 \times 10^5$.

Note that the sooting threshold in F17 was estimated at C/O = 0.70 in (Sgro et al., 2009) from the combined observation of LII signal and absorption in the visible. Flames at lower C/O were designed in (Sgro et al., 2009) as "non-sooting" and their PSDs were attributed to NOC. On the contrary, in this work soot particles heated by the laser at 1064 nm were verified to emit blackbody radiation (see section 3.2.2) for C/O greater than 0.57 in F10 and 0.59 in F17. Therefore, those flames were considered as sooting flames, in agreement with the visual threshold of (Haynes & Wagner, 1981).

3.2. LII

3.2.1. Fluence curves

The LII signal collected at 532 nm from identical soot particles with a soot volume fraction f_v is given by (Betrancourt et al., 2019):

$$LII = \Theta K\, E(m_{532}) \exp\left(-\frac{K^*}{T}\right) f_v \tag{5}$$

with $K = \frac{48\pi^2 hc^2}{\lambda_{532}^6}$ and $K^* = \frac{hc}{k_b \lambda_{532}}$. $E(m_{532})$ is the soot absorption function at the detection wavelength (532 nm), T is soot temperature and Θ the detection system constant which particularly accounts for the wavelength-independent parameters, such as the laser bandwidth, the collection solid angle and volume.

Varying the laser fluence leads to a change in the particle temperature, which is derived from the unsteady energy balance equation written for a primary particle:

$$\frac{1}{6}\pi d_p^3 \rho_s c_s \frac{dT}{dt} = c_{abs} F q(t) - q_c + \frac{\Delta H_v}{M_v}\frac{dm}{dt} \tag{6}$$

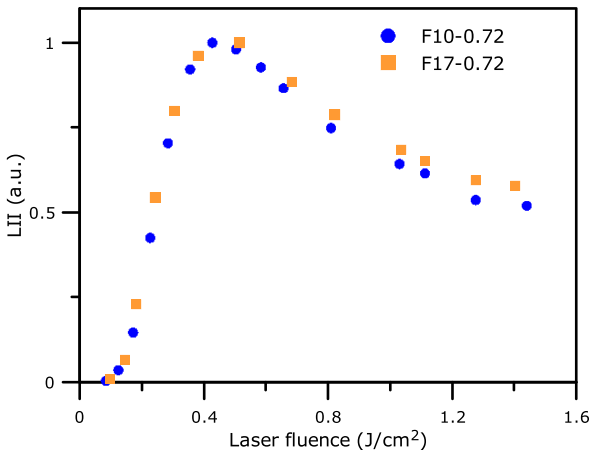

Fig. 2. Normalized LII signal as a function of the laser fluence in F10-0.72 and F17-0.72 (fluence curves).

where d_p is the primary particle diameter, ρ_s and c_s are the density and specific heat capacity of soot, t is time. C_{abs} is the absorption cross section of the primary particle evaluated using the Rayleigh regime expression at the laser wavelength ($C_{abs} = \frac{E(m)\ \pi^2 d_p^3}{\lambda}$), F is the laser fluence, $q(t)$ is the normalized laser power temporal profile, q_c is the heat loss rate due to conduction. The last term in Eq. (6) represents the sublimation heat loss rate with m being the mass of primary particle, M_v the mean molecular weight of the sublimated species, and ΔH_v the heat of sublimation.

Consequently, the variation of the LII signal as a function of the laser fluence (fluence curve) for a given soot (given d_p, ρ_s, c_s, C_{abs}) is in a way the energy signature of the soot particle.

3.2.1.1. LII fluence curves for mature soot. Fig. 2 shows the peak-normalized fluence curves of soot particles laser-heated at HAB = 16 mm in F10-0.72 and F17-0.72. The curves are very similar. The LII threshold at which the LII signal starts to increase is around 0.1 J/cm^2. The LII curves peak at around 0.4 J/cm^2 and then start to decrease due to sublimation. The similar behavior of the two flames indicates that the soot particles have close properties. The fluence curves are very similar to those reported by (Olofsson et al., 2015) in the burnt gases of F10 for a C/O ranging from 0.70 to 0.76, and therefore can be considered as "mature soot". Note that the high fluence (0.4 J/cm^2) at which LII reaches its maximum is linked to the fact that soot particles (before the laser impulsion) have a relatively low temperature (1100–1300 K, section 3.2.3) and therefore require high fluence to reach the sublimation temperature.

3.2.1.2. LII fluence curves as a function of C/O. While numerous studies have reported on the influence of the incident radiation (laser profile, wavelength) on the shape of the fluence curves (Bladh & Bengtsson, 2004; Bladh et al., 2006; Delhay et al., 2005), only few have focused on the impact of the soot properties (Johansson et al., 2017). This concerns for instance the impact of the soot maturity

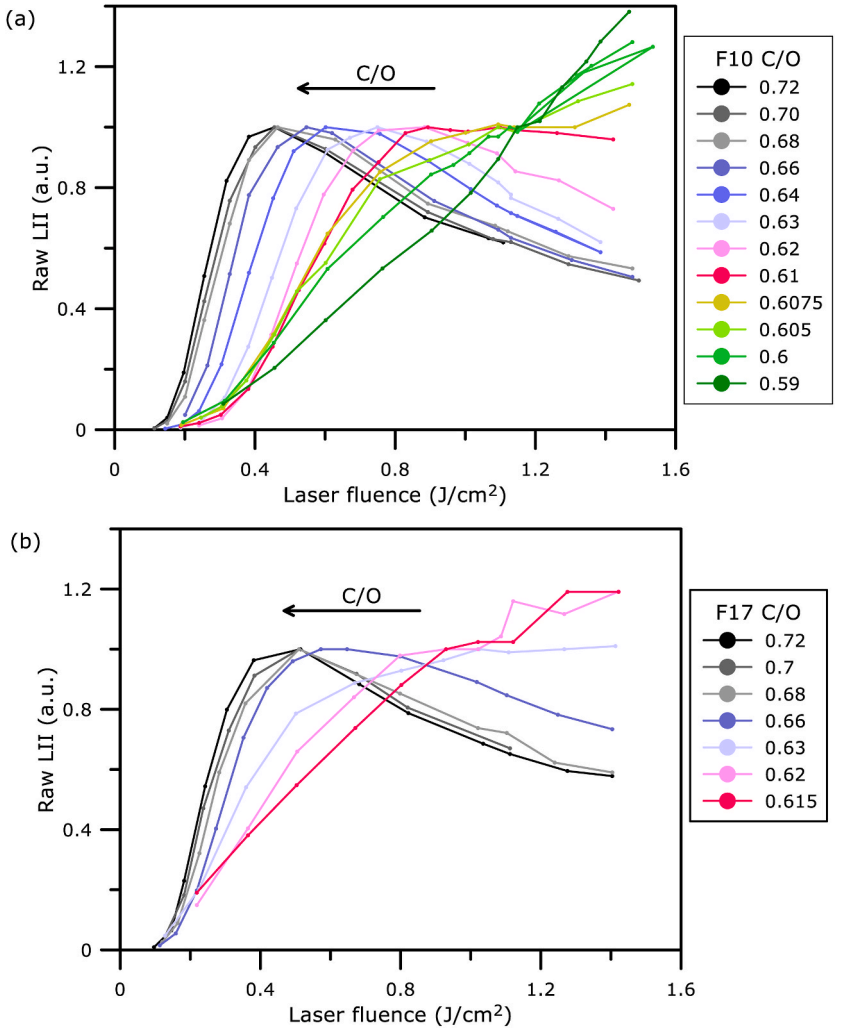

Fig. 3. Fluence curves representing the variation of the LII signal as a function of the laser fluence at 16 mm HAB in F10 (a) and F17 (b). The LII signal was normalized to the plateau value. The legend indicates the value of the C/O of each fluence curve. The lines are guidelines, not fittings.

(Eremin et al., 2020; Lemaire & Menanteau, 2021; López-Yglesias et al., 2014; Mannazhi et al., 2023; Olofsson et al., 2015), or of the C/O ratio (Betrancourt et al., 2019; Bladh et al., 2015). In the above cited works, it was shown that the younger the soot, the higher the LII threshold, i.e. the fluence curves at low HAB (young soot) were found shifted towards higher laser fluences in comparison to the fluence curves at high HAB (mature soot).

In this work, fluence curves have been measured in F10 and F17 on a wide range of C/O as shown in Fig. 3a and Fig. 3b. Similar behaviors are observed between F10 and F17 but at different C/O. They are attributed to the change of soot optical properties as C/O evolves. It is not yet clear whether this change in optical properties is due to the particle chemical composition, structure or PSD. At high C/O (0.62–0.72 for F10 or 0.66–0.72 for F17), the LII signal reaches a maximum and then decreases as for mature soot described in previous section. But the lower the C/O, the higher the LII threshold. Such behavior was observed in (Betrancourt et al., 2022; Bladh et al., 2015) but on a much narrower C/O range and in three flames only. Then, the fluence curves reach a plateau at C/O = 0.61 for F10, and at C/O = 0.63–0.64 for F17. The fluence curves have been normalized to their maximum value (reached in the plateau region). At low C/O, the LII signal first increases, flattens around 1.1 J/cm^2, and then increases again above 1.2 J/cm^2. This behavior is very evident for F10. In (Bladh et al., 2015), the fluence curve obtained in F10-0.59 suggested the start of a plateau at fluence above 1.2 J/cm^2 consistently with the present measurements. This region in which the signal first flattens was selected for normalizing the corresponding fluence curves. The change of the LII behavior at very high fluence for the lowest C/O was interpreted as resulting from strong sublimation of the soot particles, possibly accompanied by background emission (Goulay et al., 2009).

The uncertainty in the LII signal depended on the signal amplitude. To cover all the fluence curves, the PMT input voltage was set to its maximum and neutral density filters, adjusted flame by flame, were interposed in front of the PMT to avoid PMT saturation in the highest C/O flames. In F10-0.59, the signal was 150 mV on the plateau offering a very good signal to noise ratio. Consequently, the uncertainty of the LII signal at high fluence was low, estimated to around ±5% for all flames. However, at low fluence, when the signal was around 10 mV, the uncertainty increased and was estimated to ±15%.

3.2.2. *Determination of the temperature of laser-heated soot particles*

The temperature of the laser-heated soot particles was determined from the analysis of the LII spectra obtained at a fluence close to the plateau region. In most of the works available in the literature, the temperature of the laser-heated particles is determined using two-color LII (2C-LII), by collecting the incandescence at two wavelengths in the visible spectrum. The calibration is generally performed using calibrated sources. The full incandescence spectra are rarely shown because they require a more expensive and complex set-up, and are often acquired at the expense of the signal to noise ratio.

In this work, we determined the spectral signature of the radiation emitted by the laser-heated particles, especially at low C/O. The detection of blackbody emission is a fundamental criterion used to prove whether or not the particles can be classified as soot. Concretely, as detailed below, the laser-heated particles at 16 mm HAB in all the investigated flames were found to emit a blackbody radiation, and therefore were considered as soot. This assessment is consistent with the visible color to the naked eye of all these flames, which radiate from yellow-orange at high C/O to pale yellow at low C/O. The raw LII spectrum in F10-0.68 is provided in Fig. 4a.

To determine the spectral response of the detection system (spectrometer, lenses and PMT), the following approach was used: considering that the fluence curve in F10-0.72 is very similar to the one obtained by (Olofsson et al., 2015) in the same F10 (section 3.2.1.1), we assumed that the temperature of the plateau was the same than that measured by (Olofsson et al., 2015) i.e. around 4400 K. Their measurements were performed by 2C-LII at 585 and 684 nm and assuming a wavelength independent $E(m)$. Note that Goulay et al. (2013) also reported a maximum temperature around 4400 K for mature soot issued from ethylene combustion using spectrally resolved LII emission. Herein, by imposing this temperature to mature soot, and assuming a wavelength independent $E(m)$, the spectral response of the detection system could be determined. The laser fluence was adjusted to slightly above the LII peak of the fluence curve

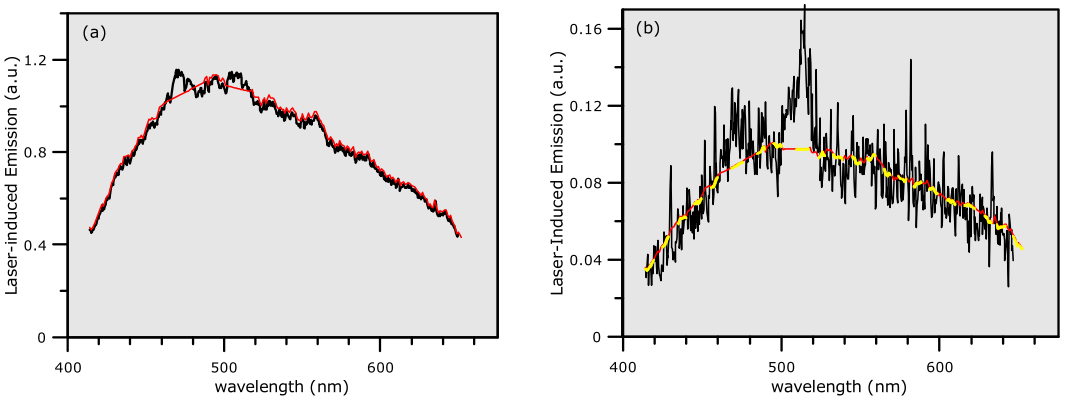

Fig. 4. Raw laser-induced emission (black line) and theoretical (red line, $E(m)$ constant with λ) spectra (a) in F10-0.68 (blackbody fitting is obtained for T = 4400 K), and (b) in F10-0.59 (blackbody fitting is obtained for T = 3960 K). The yellow fit in Fig. 4b is explained in section 3.3. It corresponds to a laser-induced emission spectrum calculated with T = 3570 K and $E(m,\lambda) = 1/\lambda^{\alpha-1}$, with α = 1.75.

for each C/O. It was found that a 25% variation in fluence did not alter the shape of the spectrum, and therefore the temperature. The fitting accuracy was estimated to ±80 K. A comparison between the experimental and theoretical spectra is shown in Fig. 4a. The (inverse) theoretical blackbody spectral response matches the experimental one at the imposed temperature (4400 K), with the exception of the two weak spectral features around 473 nm and 512 nm. These features correspond to C_2 emission due to soot sublimation at high temperature, and are similar to the spectra reported by (Goulay et al., 2009, 2013) in an ethylene/air diffusion flame. In F10-0.59 the signal to noise ratio decreases considerably (approximately by a factor 4000), but a satisfactory match was found for $T = 3960$ K (Fig. 4b). Note that the C_2 bands are much larger in this flame which may partly explain the re-augmentation of the LII signal above 1 J/cm^2 (see Fig. 3a). The (normalized) blackbody emission spectra were found unchanged in F10 from C/O = 0.72 to 0.61, meaning that the peak temperature reached around 4400 K in all cases. Then, the peak temperature was found to decrease gradually from 4200 K in F10-0.605 down to 3960 K in F10-0.59. Spectra in F17 were found similar to that in F10-0.68 for C/O > 0.63 ($T = 4400$ K) while the maximum temperature was found to be around 4200 K in F17-0.62. The signal to noise ratio was too low in leaner flames to determine the peak temperature.

3.2.3. *Interpreting the fluence curves to obtain the evolution of E(m) with C/O*

In (Betrancourt et al., 2019), LII measurements were performed in two n-butane atmospheric premixed sooting flames, including a nucleation flame. Instead of showing fluence curves (LII signal as a function of flunece), the temperature of the heated particles was plotted as a function of laser fluence up to 0.4 J/cm^2. The temperature was deduced from 2C-LII pyrometry. It was shown that the curve obtained in the leanest flame was shifted towards higher fluences in comparison with the richest flame. In the low-fluence part of the fluence curves, it was possible to rely the $\Delta T = T(t_p) - T_g$, where $T(t_p)$ is the soot temperature reached at a given fluence at the end of

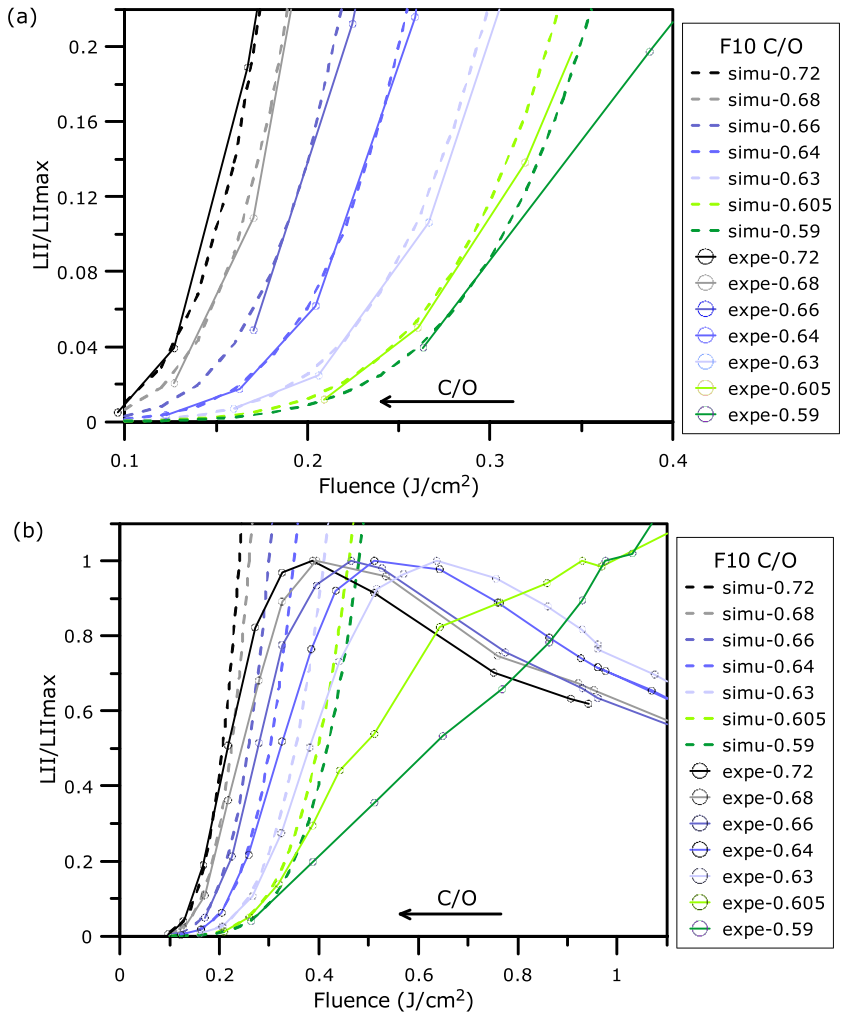

Fig. 5. Comparison between $\frac{LII}{LIImax}$ determined experimentally (continuous lines) and by calculation (dashed lines) as a function of the fluence in F10. Vertical scale in (a) is limited to 0.22 whereas the full scale is represented in (b). The number indicated in the legend represents the value of the C/O.

the laser pulse of duration t_p and T_g is the gas temperature, to $E(m_{\lambda_{laser}})$, ρ_s and $c_{s,}$ according to Eq. (7) derived from Eq. (6) in the low fluence regime (i.e. neglecting the conduction and sublimation terms):

$$\Delta T = T(t_p) - T_g = 6\pi \frac{F}{\lambda_{laser}} \frac{E(m_{\lambda_{laser}})}{\rho_s c_s} \tag{7}$$

This approach led to the determination of the variation of $\frac{E(m_{\lambda_{laser}})}{\rho_s c_s}$ between the two flames, and finally to the variation of $E(m_{\lambda_{laser}})$. It was shown that $E(m_{\lambda_{laser}})$ for the smallest soot particles (~2 nm) obtained in the leanest (nucleation) flame was 40 % lower than in the richest flame (with nearly mature soot). In (Betrancourt et al., 2019), the $E(m_{\lambda_{laser}})$ value for mature soot was imposed to 0.41.

The present work is inspired by the above-mentioned study. The first major challenge faced in this work was that the temperature could not be measured with sufficient accuracy against the fluence in all flames because f_v was 10 times lower than in (Betrancourt et al., 2019) for the leanest flames. Consequently, we adopted the following approach. The normalized LII curves of Fig. 3a and b can be expressed as:

$$\frac{LII}{LIImax} = \exp\left[-K^* \left(\frac{1}{T(t_p)} - \frac{1}{Tmax} \right) \right] \tag{8}$$

where *LIImax* is the plateau value of the LII signal (set to 1 in the previous figures), and *Tmax* is the corresponding temperature of the soot particles (this also means that, according to Eq. (7), when $T = Tmax$, the right-hand side of Eq. (8) equals to 1). In the low fluence regime, T can be determined from Eq. (7).

The gas temperature T_g was determined by solving the energy equation for a case of a burner stagnation flame in Chemkin-Ansys (Chemkin, 2021), similarly as in (Betrancourt et al., 2022). The temperature of the stabilization plate, measured with a K type thermocouple (diameter 250 μm) in each flame, was found to be 720 K in F10 and 870 K in F17, while the burner surface temperature was imposed at 600 K and 700 K in F10 and F17 respectively. The simulated temperature at HAB = 16 mm is relatively low due to the proximity of the plate, resulting in an average temperature of 1200 K in F10 and 1380 K in F17.

$T(t_p)$ was calculated using Eq. (7) by using $\rho_s c_s = 4.59\ 10^6$ J/m^{3}K given in (Johansson et al., 2017). This assumption is discussed in section 3.3. F was measured (section 2.2.1), T_g was estimated by simulation and *Tmax* determined from the LII spectra analysis (section 3.2.2). $E(m_{1064})$ is the absorption function at 1064 nm and was the only parameter adjusted for each fluence curve ($\frac{LII}{LIImax}$ as a function of F) to obtain the best match between the experimental and the theoretical LII signal given by Eq. (8). This adjustment was done at low fluence (Fig. 5a) for selected fluence curves of Fig. 3a. Fig. 5a shows a reasonable agreement between the experience and the theory. It should be pointed out that the calculation/experiment comparison was performed in the low-fluence LII regime (lower than 20 % of *LIImax*), i.e. in a region of the fluence curve that is not generally precisely documented in the literature. Thus, in F10-0.59 the signal at low fluence was only around 10 mV, meaning that the derived value of E(m) is affected by a larger uncertainty in comparison to higher C/O. Fig. 5a is extended to the higher fluences in Fig. 5b. As expected, the theoretical signal at high fluence increases indefinitely since neither sublimation nor conduction are introduced in Eq. (7). The divergence between theory and experience starts at $\frac{LII}{LIImax} = 0.4$ for high C/O and tends to gradually decrease below $\frac{LII}{LIImax} = 0.2$ at the lowest C/O. F17 were analyzed similarly as shown in Supplemental Materials SM3.

$E(m_{1064})$ values from Fig. 5a and SM3 are combined in Fig. 6 (the table of values is provided in Supplemental Materials SM4). It is important to note that the method developed herein does not rely on the choice of a reference value of $E(m_{1064})$ in a selected flame, but directly provides the absolute value. This method is close to the alternative LII modeling used to deduce the soot absorption function, which was also carried out in the low fluence regime, meaning that conduction and sublimation were neglected. It should be noted,

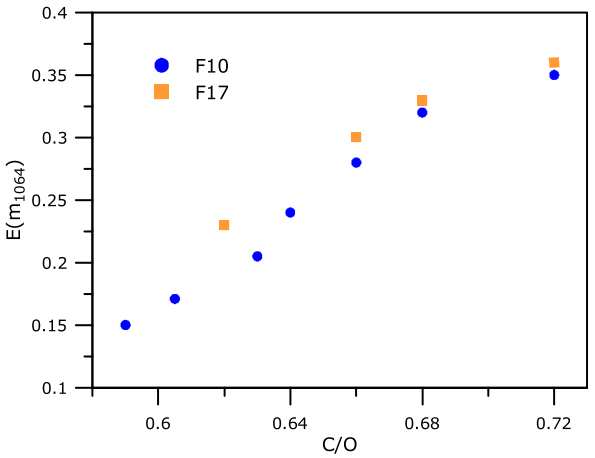

Fig. 6. $E(m_{1064})$ *as a function of C/O in F10 and F17.*

however, that LII modeling requires the particle diameter as an input unlike the method proposed in the present work. As expected from Fig. 2, $E(m_{1064})$ in F10-0.72 and F17-0.72 are very close, respectively 0.35 and 0.36, which is in the range of generally adopted values for mature soot. Regardless of the flame (F10 or F17), $E(m_{1064})$ decreases similarly with C/O, down to 0.15 in F10-0.59. In (Betrancourt et al., 2019), $E(m_{1064})$ was found to vary from 0.41 (imposed value) to 0.25 in the burnt gases of n-butane sooting premixed flames for C/O ranging from 0.60 to 0.54. Note that the trend of $E(m_{1064})$ decrease with C/O seems to be unaffected by the total flow rate of the present ethylene flames.

The determination of $E(m_{1064})$, based on the best agreement between calculated and experimental fluence curves, is multi-parameter and depends on the accuracy of $T(t_p)$ determination. From a theoretical point of view, the sensitive parameters for determining $T(t_p)$ are T_g , $\rho_s c_s$ and fluence F. What emerged from the calculations is that any deviation in these parameter values led to a constant deviation in all values of $E(m_{1064})$ as a function of C/O. Considering that $E(m_{1064})$ obtained for F10-0.72 and F17-0.72 is in line with the literature, we believe that our parameter selection is correct. Given the ±10% uncertainty in the experimental fluence, which is reflected in the $E(m_{1064})$ selection of the theoretical fluence curves, we estimated the $E(m_{1064})$ uncertainty to be ±15% for the high C/O, gradually increasing to ±30% for the lowest C/O of F10 and F17.

As shown in Table 2, the $E(m_{1064})$ is globally in agreement with previous in situ determination using in situ LII but shows important discrepancies with ex situ diagnostics. The $E(m_{1064})$ of incipient soot or very small soot particles, determined using in situ LII, is found to be between 0.15 and 0.25, i.e. 1.6 to 2.7 times lower than $E(m_{1064}) = 0.40$ often used for mature soot. The similar range of values of $E(m_{1064})$ found for both incipient soot and very small soot particles does not mean that these particles are identical. Structure and chemical composition of incipient particles found at the onset of the soot region and partially matured soot particles found in the burned gases might differ significantly. However, the convergence of the results found in this work indicates that the change in particle maturity has a smaller impact on the optical properties of incipient soot and very small soot than the particle size. This discussion is completed in section 3.3. This low but still consequent value of $E(m_{1064})$ explains why incipient soot (at the onset of soot formation), or very small soot particles (all along the nucleation flames) can be detected in situ by LII or absorption (see Eqs. (4) and (5)) even though the f_v is very low. In (Bocchicchio et al., 2022), the values reported in Table 2 depend on the choice of ρ. Referring to the commonly adopted value of ρ for incipient soot (1.2 g cm^{-3}), one obtains $E(m_{678}) = 0.07$ which is closer to the in situ values but still much lower. At this stage, we believe that the differences observed between in situ and ex situ determination of $E(m)$ could be inherent to the sampling or soot deposition. This aspect is discussed in (Bocchicchio et al., 2022) where the authors advocate for the introduction of a

Table 2
Non-exhaustive summary of absolute $E(m)$ measurements. The table only includes works carried out on premixed atmospheric burner-stabilized flames, including incipient soot and very small soot particles. Some of these works are detailed in section 2.1. The size is obtained using various techniques: microscopy TEM and HIM, SMPS, LII. v: cold gas velocity. (a) In situ optical diagnostics, (b) ex situ optical diagnostics.

	Method	Flames	Size (diameter d)	Result
Bladh 2011 (a)	LII $\lambda_{laser} = 1064$ nm	C_2H_4/air φ = 2.1 (F10, this work). v = 5.9 cm s^{-1}	Starting from 3 nm (6 mm) to 15 nm (17 mm). LII and TEM	$E(m)$ profile along the flame from 0.2 (6 mm) to 0.45 (17 mm)
Olofsson 2015 (a)	LII $\lambda_{laser} = 1064$ nm	C_2H_4/air φ = 2.1 and 2.3 (F10, this work). v = 5.9 cm s^{-1}	Starting from 3 nm (6 mm) to 15 nm (17 mm). LII and TEM	$E(m)$ varies from 0.19 to 0.22 (8 mm) to 0.34 (14 mm)
Betrancourt 2017 (a)	LII $\lambda_{laser} = 1064$ nm	$C_4H_{10}/O_2/N_2$ φ = 1.75 (nucleation flame) and φ = 1.95. v = 4 cm s^{-1}	Size around 2.5–3.5 nm at φ = 1.75. d = 3 nm at 3.5 mm at φ = 1.95. HIM and SMPS	Incipient soot at 3.5 mm at φ = 1.95 and soot along the nucleation flame have same size distribution and thermal and optical properties: E(m) = 0.25 ± 0.02
Betrancourt 2022 (a)	LII $\lambda_{laser} = 1064$ nm	$C_4H_{10}/O_2/N_2$. φ = 1.75 (nucleation flame) and φ = 1.95. v = 4 cm s^{-1}	Size around 2.5–3.5 nm at φ = 1.75. d = 3 nm at 3.5 mm at φ = 1.95. d = 10.5 nm at 10 mm at φ = 1.95. HIM and SMPS	$E(m)$ is found constant = 0.25 at φ = 1.75 and varies from 0.25 (incipient soot) to 0.41 at HAB = 10 mm of Flame1.95
This work (a)	LII $\lambda_{laser} = 1064$ nm	C_2H_4/air. φ = 1.77 to 2.16 (F10) and φ = 1.83 and 2.04 (F17). v = 5.9 cm s^{-1}, F10 and v = 10 cm s^{-1}, F17	Single mode at 2.2–2.5 nm from φ = 1.74 to 1.785 (F10-0.58 to F10-0.595) in F10. Second mode up to 6 nm from F10-0.6 to F10-0.61. Single mode at 3–4 nm in F17-0.62. Second mode from F17-0.625 to F17-0.64. SMPS	$E(m)$ from 0.15 to 0.35 (F10) and from 0.23 to 0.36 (F17) at HAB = 16 mm.
Wan 2021 & Liu 2019 (b)	Modeling of photoemission yields and absorption spectra	$C_2H_4/O_2/N_2$ flames. v from 8 to 10 cm s^{-1}	Modelling	$E(m)$ at 1064 nm decreases by a factor 20 from dp = 32 nm to dp = 5 nm (imaginary part k varies from 0.425 to 0.02)
Bocchicchio 2022 (b)	MAC determination at 678 nm	C_2H_4/air, variable φ v = 10 cm s^{-1}	d = 2 nm at φ = 1.83 at 15 mm (C/O = 0.61), d = 3.2 nm at 6 mm and 11.5 nm at 12 mm at φ = 2.16 (C/O = 0.72). SMPS	Assuming ρ = 1.8 g/cm3 for mature soot and 1.2 g/cm3 for incipient soot, E(m) varies from 0.067 (incipient) to 0.39 (mature)
Minutolo 2023 (a) and (b)	UV–vis–NIR ex situ absorption combined with in situ absorption/ scattering at 266 nm	C_2H_4/air φ = 2.01 (C/O = 0.67) v = 10 cm s^{-1}	d = 2.2 nm at 8 mm. SMPS	$E(m)$ varies from 0.52 at 200 nm to 0.02 at 1064 nm at 8 mm

correction for multiple scattering in the substrate. Another possible source could be the dependence in temperature for such very small soot particles.

To conclude, the $E(m)$ of very small soot particles obtained in this work is consistent with the previously reported values obtained by LII. The originality presented here is that this determination does not require LII modeling and assumption on the primary particle diameter but relies on the quality of the LII fluence curves, particularly in the low fluence range, and on a simple calculation (eqs. (6) and (7)) where $E(m_{1064})$ is the variable.

3.3. Comparison of the dynamic of CRDE and LII for soot volume fraction measurement

The evolution of f_v was studied by LII and CRDE as a function of C/O at 16 mm HAB in F10 (Fig. 7) and F17 (Supplemental Materials SM5). The study, which covered f_v dynamics of three orders of magnitude, had never been explored before.

f_v was obtained by CRDE from the measured extinction coefficient as explained in section 2.2.2 and from Eq. (4) with $\lambda = 1064$ nm. Therefore, f_v was easily obtained from the measurement of the cavity decay time τ_{soot} by applying the value of $E(m_{1064})$ determined in section 3.2.3 (Fig. 6). τ_{soot} and the flame diameter were each determined with a precision better than 2%. The greatest uncertainty in the determination of f_v was due to $E(m_{1064})$ as mentioned above. Consequently, the uncertainty in the CRDE determination of f_v was $\pm$20% for high C/O, gradually increasing to $\pm$35% for the lowest C/O of F10 and F17.

By contrast, extracting f_v from the LII signal was more complex as shown in Eq. (5). First, being Θ unknown, the LII signal needed to be calibrated against an absolute value obtained independently. Second, the signal is dependent on the temperature reached by the laser-heated soot particle as shown in Eq. (5) that in turns depends on the volumetric heat capacity $\rho_s c_s$ as shown in Eq. (7). Both dependences in T and $\rho_s c_s$ contribute to increase the uncertainty on f_v. Concerning the dependence of the signal on $E(m)$, values at 532 nm should be used. We assumed that $E(m_{532})$ and $E(m_{1064})$ evolve similarly over the range of soot investigated. This is reasonable considering the literature (López-Yglesias et al., 2014; Therssen et al., 2007). Note that this assumption relies only on the relative variation of $E(m_{532})$, and not on its absolute value. Indeed, the calibration proposed above overcomes the lack of knowledge of $E(m_{532})$.

In what follows, we first look at the dynamics of the two techniques over 3 orders of magnitude of f_v. In Fig. 7, the f_v extracted from CRDE (open squares, left axis) and the raw LII signals (solid circles, right axis) were corrected for the variation of $E(m)$ over the range of C/O using values determined from the methodology explained in section 3.2.3. Both curves are arbitrarily scaled at C/O = 0.63. The $E(m)$, which were not determined using this procedure, were obtained by interpolating or extrapolating the values shown in Fig. 6 as follows: since E(m) monotonically increases from 0.59 up to 0.66 C/O, we performed a linear interpolation to obtain the missing $E(m)$ values required for Fig. 7. Below C/O = 0.59, we have extended the $E(m)$ trend shown in Fig. 6. The values of $E(m)$ are reported in SM4. The error associated to the extrapolation is estimated to $\pm$30 % at C/O = 0.57. The signal variations issued from both techniques have a similar behavior for C/O $\geq$ 0.61. Below this C/O, the lower C/O and the greater the gap between LII and CRDE. By correcting the LII signal for the variation in temperature of the laser-heated soot, in the range where temperatures were measured, the deviation could be partially compensated (open blue circles). A similar trend between LII and CRDE would require to correct the LII signal by introducing a much lower temperature than the measured one. For example, for C/O = 0.59, the ideal correction would require a soot temperature of 3570 K while the measured one is 3960 K. In our calculations (Eq. (7)), we assumed a constancy of the volumetric heat capacity $\rho_s c_s$. However, it has been shown that while $\rho_s c_s$ of a single-crystal graphite tends to 4.59 10^6 J/m^{3}K at high temperature, it gradually decreases at low temperatures (Michelsen, 2021). In this work, this dependency was neglected. This would certainly have an impact on the position of the fluence curves, and therefore on the determined $E(m)$. But the impact would be similar on both CRDE and LII trends.

Globally, an excellent agreement between LII and CRDE was found in F10 with C/O $\geq$ 0.61 and in F17 for C/O $\geq$ 0.63 (see Supplemental Materials SM5). Note that these two ranges of C/O correspond to flames where the particle temperature was close to that of mature soot (4400 K). At lower C/O, a gradual deviation is observed: a likely explanation is that we implicitly considered that spectral emissivity was not affected by soot particle size or maturity for the determination of temperature. (Olofsson et al., 2015)

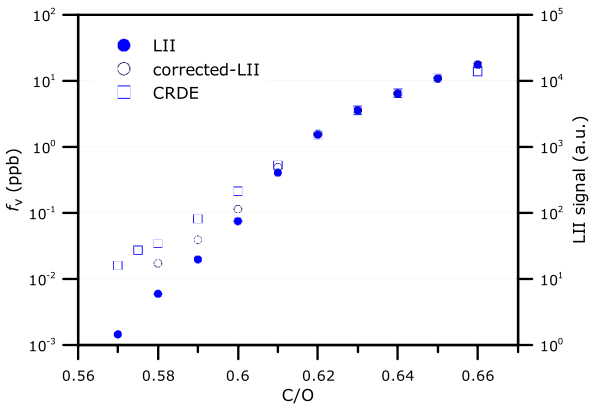

Fig. 7. Comparison between CRDE (open squares) and raw LII (solid circles) as a function of C/O in F10. The open circles represent the LII signal corrected for the temperature using Eq. 5.

showed that incorporating a dispersion coefficient α (cf. section 2.1) considerably reduced the calculated temperature of the laser-heated soot particles. Their correction is issued from (Simonsson et al., 2015) performed in F10-0.70 and where α was found to vary from 4 at low HAB to 1 in the burnt gases. Applying the variation of α to $E(m)$ at the two detection wavelengths led to temperature corrections as large as 1000 K at low HAB. Based on (Olofsson et al., 2015; Simonsson et al., 2015), the most likely explanation for the divergent trends in LII and CRDE at low C/O (meaning for soot probably having similar optical properties as those found at low HAB in F10-0.7) is the failure to take into account the spectral dependence of emissivity when calculating the temperature. Unfortunately, it is difficult to apply the attractive approach from the group of Lund (based on single-path absorption at different wavelengths provided by "simple" continuous-wave laser diodes) to our flames because of the very low f_v which requires CRDE for measuring the soot absorption. To assess the impact of a possible spectral dependence of $E(m)$ on the determination of the temperature of the laser-heated soot particle, we proceeded as follows: instead of extracting the temperature (3960 K) from the laser-induced emission spectrum in Fig. 4b (C/O = 0.59) by fixing a constant value of $E(m)$ with wavelength, the temperature was fixed to the value T = 3570 K that allowed the best agreement between CRDE and LII at C/O = 0.59 (see Fig. 7) and α was varied until a good agreement between calculated and experimental spectra was reached. The spectrum obtained with T = 3570 K and α = 1.75 is shown in Fig. 4b. It is noteworthy that the emission spectrum fitted by $I_{bb}(T) \times E(m)/\lambda$, where $I_{bb}(T)$ is the Planck blackbody spectral radiation intensity (Betrancourt et al., 2019) and $E(m)$ is fixed, coincides with the spectrum fitted by $I_{bb}(T) \times E(m,\lambda)/\lambda$ with $E(m,\lambda) = 1/\lambda^{\alpha-1}$. Of course, in both cases, the derived temperatures are different. The obtained $\alpha > 1$ is in line with the literature, although not as high as in (Simonsson et al., 2015) for incipient soot.

Our work identifies that the discrepancy between CRDE and LII occurs in F10 with C/O < 0.61 and in F17 for C/O < 0.63. It is interesting to note that, as suggested above, this discrepancy would originate from a spectral dependence of $E(m)$ in this range of C/O but not from a variation of $E(m)$ at fixed wavelength (which monotonically increases with C/O as shown in Fig. 6). It is noteworthy that the PSDs in this range of C/O are dominated by the first mode. This lets us suggest that the optical properties of bigger soot particles dominated by the second mode have a weak spectral dependence, in contrast with very small soot particles (<6 nm), with an important single mode which could correspond to soot particles with a large spectral dependence of their optical properties. In turns, this suggests that the presence of an important single mode drives the spectral dependence of $E(m)$ of very small soot particles.

In order to evaluate the reliability of f_v measurements, in Fig. 8 we compared the f_v profiles of flame F10-0.70 obtained by single-path extinction in (Simonsson et al., 2015) and by CRDE obtained in this work. To make the comparison we used the same value (0.35) of $E(m)$ as in (Simonsson et al., 2015) all along the flame profile. In the burnt gases, the f_v agrees within 30 % and the overall shape of the profiles are very similar. The CRDE data are more reliable and sensitive at low f_v. A dynamic range of around 500 of f_v is found along the profile measured by CRDE. It must be noted that the 10^{-4} accuracy for single path extinction reported in (Simonsson et al., 2015) is remarkably high for single-path extinction. Finally, we recorded the f_v profile in F10-0.59 flame. As previously shown in (Bladh et al., 2015), this flame is a nucleation flame and the LII decay times along the flame are nearly constant (see Supplemental Materials SM1). According to Fig. 1, the PSD mode is at 2.3 nm, in close agreement with previous size determination in nucleation flames (Betrancourt et al., 2019, 2022; Do et al., 2021). The constancy of the LII decay time indicates that the soot growth is nearly inexistent. This explains the limited 3-fold increase of f_v (in comparison with 500-fold in F10-0.70) consistently with previously reported f_v profiles in nucleation flames (Betrancourt et al., 2019, 2022; Do et al., 2021). This small increase of the f_v results from a very slight soot growth of the soot particles formed at the onset of the soot profile combined to a continuous production of incipient soot particles along the HAB (due to soot precursors presence) (Aubagnac-Karkar et al., 2018). This profile is found very similar to the one obtained in F17-0.62. This illustrates that the cold gas velocity has a strong impact on the soot formation. When velocity increases from 5.9 cm s^{-1} to 10 cm s^{-1} the f_v in atmospheric C_2H_4/air flames stabilized on a porous burner decreases by around a factor of 10 at constant C/O. Although we did not measure the f_v profile in F17-0.67, we could compare the value of f_v in the burnt gases. We found at 16 mm f_v = 3.1 ppb using $E(m)$ = 0.3, which is 20 times lower than the value determined by ex situ SMPS at 14 mm (Commodo et al.,

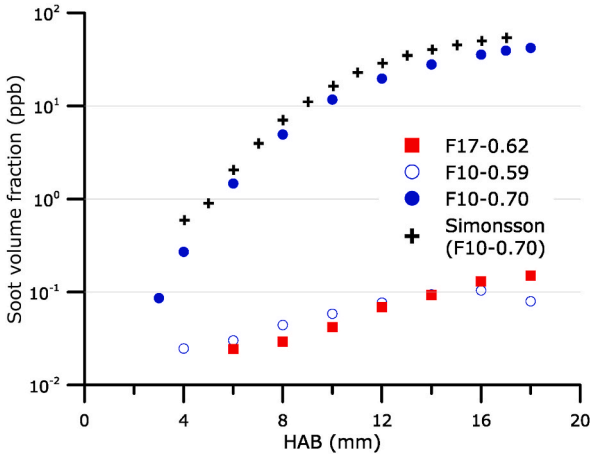

Fig. 8. *f_v profiles obtained in several F10-F17 flames. The $E(m_{1064})$ was set to 0.35 in F10-0.70, to 0.15 in F10-0.59 and to 0.23 in F17-0.62.*

2015).

Finally, it is noteworthy that LII and CRDE have a similar limit of detection in the ppt range in F10 and F17, keeping in mind that the measurement volume in CRDE is roughly one fifth of the LII volume.

4. Conclusion

In this work, we compared and combined LII and CRDE to measure the soot volume fraction (f_v) at 16 mm HAB in several premixed ethylene/air flames stabilized on a porous burner. The C/O ratio was varied on a large range and two flow rates (F10 and F17) were investigated. The selected flames offer a variation of f_v of 3 orders of magnitude at HAB = 16 mm. SMPS experiments were performed to obtain the soot particle size distributions (PSDs), that are monomodal at low C/O and evolve to bimodal at higher C/O. LII and CRDE experiments were performed at 1064 nm. The set-up of both techniques was arranged to obtain the highest sensitivity. It was found that the detection limit of both techniques was similar around a few ppt in f_v.

In all investigated flames, laser-induced emission spectra revealed that particles emit blackbody radiation, justifying the attribution of absorption and laser-induced emission (LII) at 1064 nm to soot particles. The temperature of the laser-heated particles was determined from the analysis of the spectrally resolved laser-induced emission spectra.

The determination of the absolute value of $E(m)$ and of its variation in the flames was derived from an original analysis of the LII fluence curves recorded up to 1.4 J/cm^2. Fluence curves were shown to be strongly dependent on C/O, revealing that the optical properties of soot are subject to important variations. For each fluence curve, which shows the LII signal as a function of the laser fluence F, it was shown that dividing the *LII* signal by its value at the plateau of the fluence curve (*LIImax*, reaching the temperature *Tmax*) leads to the simplified expression: $\frac{LII}{LIImax} = \exp\left[-K^*\left(\frac{1}{T(t_p)} - \frac{1}{Tmax}\right)\right]$, where $T(t_p)$ is the temperature reached by the soot particle at fluence F. This last temperature was calculated in the low fluence regime, using $T(t_p) = T_g + 6\pi\frac{F}{\lambda_{laser}}\frac{E(m_{\lambda_{laser}})}{\rho_s c_s}$ where the gas temperature T_g was determined by flame modeling and $\rho_s c_s = 4.59\ 10^6$ J/m^{3}K. The soot absorption function $E(m_{\lambda_{laser}})$ at 1064 nm was the only parameter adjusted for each fluence curve ($\frac{LII}{LIImax}$ as a function of F) to obtain the best match between the experimental and the theoretical fluence curves. From this procedure, independent on the knowledge of the soot particle diameter, the absolute value of $E(m)$ could be determined in the flames. At high C/O, $E(m)$ was found to be 0.35–0.36, consistently with the literature. In F10, $E(m)$ decreased down to 0.15 in F10-0.59. A similar decrease of $E(m)$ with C/O was observed independently of the flow rate. Although the absorption function of the smallest soot particles is indeed much lower than that of mature soot (here up to 60% less), it is still sufficient to allow measurable absorption of the smallest soot particles at 1064 nm down to a limit of detection of a few ppt in f_v. This result is in disagreement with other literature works (C. Liu et al., 2019; Minutolo et al., 2023; Wan et al., 2021), where the $E(m)$ of these particles in the near IR is found to be extremely low, down to 0.02. This discrepancy merits further investigation: the particles analyzed in the mentioned works might have different structure or chemical composition, or the sampling, required for ex situ investigations, might have altered their optical properties.

The present study also reported for the first time a comparison of the dynamic of LII and CRDE, over a very wide range of three orders of magnitude of f_v, which includes very small soot particles of 2–4 nm. The interpretation of CRDE decay times relied solely on the determination of $E(m)$, obtained from the previous analysis, and gave the absolute f_v. In contrast, the LII is highly temperature-dependent and only gave access to the relative value of f_v. A very good agreement between LII and CRDE was found over a dynamic range of f_v of around two orders of magnitude, above C/O = 0.61 and 0.63 in F10 and F17, respectively. For these flames, the temperature of the laser-heated soot particles was similar around 4400 K. However, below these two C/O limits, for smaller soot particles, a gradual deviation was found between both techniques, LII exhibiting a stronger decrease with C/O in comparison with CRDE. This deviation was partially compensated when correcting the LII signal for the temperature variation of the laser-heated soot particles but was still insufficient. This persistent discrepancy is probably due to the fact that no spectral dependence of emissivity was taken into account in the temperature calculation. We observed that the above-mentioned deviation occurs at C/O for which the PSD is dominated by the first mode. This suggests that the presence of an important single mode drives the spectral dependence of $E(m)$ of very small soot particles, while the second mode would have a weaker spectral dependence. The comparison of the variation in absorption and LII of 2–4 nm soot particles in different flames could pave the way for a future method of determining the dispersion coefficient α of 2–4 nm soot particles, which affects LII, by adjusting this coefficient to obtain the same signal dynamics between the 2 techniques. For instance, for F10-0.59, a good agreement between the techniques requiring a temperature of 3570 K could be obtained by fixing α = 1.75. In conclusion, this study proposes a robust methodology based on combined LII and CRDE measurements to obtain both in situ E(m) and f_v measurements without complex LII modeling and applicable to a wide range of soot particles, in terms of concentration and size, notably including 2–4 nm soot particles. Further work will focus on the quantitative comparison of soot volume fraction between CRDE and SMPS.

CRediT authorship contribution statement

Pascale Desgroux: Writing – review & editing, Writing – original draft, Supervision, Methodology, Investigation, Funding acquisition, Conceptualization. **Nathalie Lamoureux:** Software, Formal analysis. **Alessandro Faccinetto:** Writing – review & editing, Methodology, Investigation, Formal analysis.

Declaration of competing interest

The authors declare that they have no known competing financial interests or personal relationships that could have appeared to influence the work reported in this paper.

Data availability

Data will be made available on request.

Acknowledgments

This work is a contribution to the LabEx CaPPA (ANR-11-LABX-0005-01) projects funded by the French National Research Agency, to the CPER research project ECRIN funded by the French Ministère de l'Enseignement Supérieur et de la Recherche and to MéOL plateforme of Univ. Lille. The authors thank the Regional Council "Hauts-de-France" and the "European Regional Development Fund".

Appendix A. Supplementary data

Supplementary data to this article can be found online at https://doi.org/10.1016/j.jaerosci.2024.106385.

References

ANSYS Chemkin R1 Inc (2021 R1). (2021). [Computer software]. ANSYS, Inc.

Appel, J., Bockhorn, H., & Frenklach, M. (2000). Kinetic modeling of soot formation with detailed chemistry and physics: Laminar premixed flames of C2 hydrocarbons. *Combustion and Flame, 121*(1), 122–136. https://doi.org/10.1016/S0010-2180(99)00135-2

Aubagnac-Karkar, D., El Bakali, A., & Desgroux, P. (2018). Soot particles inception and PAH condensation modelling applied in a soot model utilizing a sectional method. *Combustion and Flame, 189*, 190–206. https://doi.org/10.1016/j.combustflame.2017.10.027

Bejaoui, S., Batut, S., Therssen, E., Lamoureux, N., Desgroux, P., & Liu, F. (2015). Measurements and modeling of laser-induced incandescence of soot at different heights in a flat premixed flame. *Applied Physics B, 118*(3). https://doi.org/10.1007/s00340-015-6014-3. Article 3.

Betrancourt, C., Aubagnac-Karkar, D., Mercier, X., El-Bakali, A., & Desgroux, P. (2022). Experimental and numerical investigation of the transition from non sooting to sooting premixed n-butane flames, encompassing the nucleation flame conditions. *Combustion and Flame, 112172*. https://doi.org/10.1016/j.combustflame.2022.112172

Betrancourt, C., Liu, F., Desgroux, P., Mercier, X., Faccinetto, A., Salamanca, M., Ruwe, L., Kohse-Höinghaus, K., Emmrich, D., Beyer, A., Gölzhäuser, A., & Tritscher, T. (2017). Investigation of the size of the incandescent incipient soot particles in premixed sooting and nucleation flames of n-butane using LII, HIM, and 1 nm-SMPS. *Aerosol Science and Technology, 51*(8), 916–935. https://doi.org/10.1080/02786826.2017.1325440

Betrancourt, C., Mercier, X., Liu, F., & Desgroux, P. (2019). Quantitative measurement of volume fraction profiles of soot of different maturities in premixed flames by extinction-calibrated laser-induced incandescence. *Applied Physics B, 125*(1), 16. https://doi.org/10.1007/s00340-018-7127-2

Bladh, H., & Bengtsson, P.-E. (2004). Characteristics of laser-induced incandescence from soot in studies of a time-dependent heat- and mass-transfer model. *Applied Physics B, 78*(2), 241–248. https://doi.org/10.1007/s00340-003-1362-9

Bladh, H., Bengtsson, P.-E., Delhay, J., Bouvier, Y., Therssen, E., & Desgroux, P. (2006). Experimental and theoretical comparison of spatially resolved laser-induced incandescence (LII) signals of soot in backward and right-angle configuration. *Applied Physics B, 83*(3), 423–433. https://doi.org/10.1007/s00340-006-2197-y

Bladh, H., Johnsson, J., Olofsson, N.-E., Bohlin, A., & Bengtsson, P.-E. (2011). Optical soot characterization using two-color laser-induced incandescence (2C-LII) in the soot growth region of a premixed flat flame. *Proceedings of the Combustion Institute, 33*(1), 641–648. https://doi.org/10.1016/j.proci.2010.06.166

Bladh, H., Olofsson, N.-E., Mouton, T., Simonsson, J., Mercier, X., Faccinetto, A., Bengtsson, P.-E., & Desgroux, P. (2015). Probing the smallest soot particles in low-sooting premixed flames using laser-induced incandescence. *Proceedings of the Combustion Institute, 35*(2). https://doi.org/10.1016/j.proci.2014.06.001. Article 2.

Bocchicchio, S., Commodo, M., Sgro, L. A., Chiari, M., D'Anna, A., & Minutolo, P. (2022). Thermo-optical-transmission OC/EC and Raman spectroscopy analyses of flame-generated carbonaceous nanoparticles. *Fuel, 310*, Article 122308. https://doi.org/10.1016/j.fuel.2021.122308

Bouvier, Y., Mihesan, C., Ziskind, M., Therssen, E., Focsa, C., Pauwels, J. F., & Desgroux, P. (2007). Molecular species adsorbed on soot particles issued from low sooting methane and acetylene laminar flames: A laser-based experiment. *Proceedings of the Combustion Institute, 31*(1), 841–849. https://doi.org/10.1016/j.proci.2006.08.036

Camacho, J., Liu, C., Gu, C., Lin, H., Huang, Z., Tang, Q., You, X., Saggese, C., Li, Y., Jung, H., Deng, L., Wlokas, I., & Wang, H. (2015). Mobility size and mass of nascent soot particles in a benchmark premixed ethylene flame. *Combustion and Flame, 162*(10), 3810–3822. https://doi.org/10.1016/j.combustflame.2015.07.018

Carbone, F., Gleason, K., & Gomez, A. (2017). Probing gas-to-particle transition in a moderately sooting atmospheric pressure ethylene/air laminar premixed flame. Part I: Gas phase and soot ensemble characterization. *Combustion and Flame, 181*, 315–328. https://doi.org/10.1016/j.combustflame.2017.01.029

Cecere, D., Sgro, L. A., Basile, G., D'Alessio, A., D'Anna, A., & Minutolo, P. (2002). Evidence and characterization of nanoparticles produced in nonsooting premixed flames. *Combustion Science and Technology, 174*(11–12), 377–398. https://doi.org/10.1080/00102200215079

Choi, M. Y., Mulholland, G. W., Hamins, A., & Kashiwagi, T. (1995). Comparisons of the soot volume fraction using gravimetric and light extinction techniques. *Combustion and Flame, 102*(1), 161–169. https://doi.org/10.1016/0010-2180(94)00282-W

Commodo, M., De Falco, G., Bruno, A., Borriello, C., Minutolo, P., & D'Anna, A. (2015). Physicochemical evolution of nascent soot particles in a laminar premixed flame: From nucleation to early growth. *Combustion and Flame, 162*(10), 3854–3863. https://doi.org/10.1016/j.combustflame.2015.07.022

D'Anna, A. (2009). Combustion-formed nanoparticles. *Proceedings of the Combustion Institute, 32*(1). https://doi.org/10.1016/j.proci.2008.09.005. Article 1.

D'Anna, A., D'Alessio, A., & Minutolo, P. (1994). Spectroscopic and chemical characterization of soot inception processes in premixed laminar flames at atmospheric pressure. In H. Bockhorn (Ed.), *Soot Formation in combustion* (pp. 83–103). Springer-Verlag.

Delhay, J., Bouvier, Y., Therssen, E., Black, J. D., & Desgroux, P. (2005). 2D imaging of laser wing effects and of soot sublimation in laser-induced incandescence measurements. *Applied Physics B, 81*(2), 181–186. https://doi.org/10.1007/s00340-005-1911-5

Desgroux, P., Faccinetto, A., Mercier, X., Mouton, T., Karkar, D. A., & El Bakali, A. (2017). Comparative study of the soot formation process in a "nucleation" and a "sooting" low pressure premixed methane flame. *Combustion and Flame, 184*, 153–166. https://doi.org/10.1016/j.combustflame.2017.05.034

Desgroux, P., Mercier, X., Lefort, B., Lemaire, R., Therssen, E., & Pauwels, J. F. (2008). Soot volume fraction measurement in low-pressure methane flames by combining laser-induced incandescence and cavity ring-down spectroscopy: Effect of pressure on soot formation. *Combustion and Flame, 155*(1–2), 289–301. https://doi.org/10.1016/j.combustflame.2008.05.016

Desgroux, P., Mercier, X., & Thomson, K. A. (2013). Study of the formation of soot and its precursors in flames using optical diagnostics. *Proceedings of the Combustion Institute, 34*(1), 1713–1738. https://doi.org/10.1016/j.proci.2012.09.004

Do, H.-Q., Faccinetto, A., Tran, L.-S., Desgroux, P., Gasnot, L., El Bakali, A., & Mercier, X. (2022). Hydrogen as a fuel additive in laminar premixed methane flames: Impact on the nucleation and growth of soot particles. *Fuel, 315*, Article 123125. https://doi.org/10.1016/j.fuel.2021.123125

Do, H.-Q., Tran, L.-S., Gasnot, L., Mercier, X., & El Bakali, A. (2021). Experimental study of the influence of hydrogen as a fuel additive on the formation of soot precursors and particles in atmospheric laminar premixed flames of methane. *Fuel, 287*, Article 119517. https://doi.org/10.1016/j.fuel.2020.119517

Eremin, A. V., Gurentsov, E. V., & Kolotushkin, R. N. (2020). The change of soot refractive index function along the height of premixed ethylene/air flame and its correlation with soot structure. *Applied Physics B, 126*(8). https://doi.org/10.1007/s00340-020-07426-3. Article 8.

Forestieri, S. D., Helgestad, T. M., Lambe, A. T., Renbaum-Wolff, L., Lack, D. A., Massoli, P., Cross, E. S., Dubey, M. K., Mazzoleni, C., Olfert, J. S., Sedlacek III, A. J., Freedman, A., Davidovits, P., Onasch, T. B., & Cappa, C. D. (2018). Measurement and modeling of the multiwavelength optical properties of uncoated flame-generated soot. *Atmospheric Chemistry and Physics, 18*(16), 12141–12159. https://doi.org/10.5194/acp-18-12141-2018

Frenklach, M. (2002). Reaction mechanism of soot formation in flames. *Physical Chemistry Chemical Physics, 4*(11). https://doi.org/10.1039/B110045A. Article 11.

Frenklach, M., & Mebel, A. M. (2020). On the mechanism of soot nucleation. *Physical Chemistry Chemical Physics, 22*(9), 5314–5331. https://doi.org/10.1039/D0CP00116C

Goulay, F., Schrader, P. E., López-Yglesias, X., & Michelsen, H. A. (2013). A data set for validation of models of laser-induced incandescence from soot: Temporal profiles of LII signal and particle temperature. *Applied Physics B, 112*(3), 287–306. https://doi.org/10.1007/s00340-013-5504-4

Goulay, F., Schrader, P. E., Nemes, L., Dansson, M. A., & Michelsen, H. A. (2009). Photochemical interferences for laser-induced incandescence of flame-generated soot. *Proceedings of the Combustion Institute, 32*(1), 963–970. https://doi.org/10.1016/j.proci.2008.05.030

Hagen, F. P., Vlavakis, P., Seitz, M., Klövekorn, T., Bockhorn, H., Suntz, R., & Trimis, D. (2023). Soot nanoparticle sizing in counterflow flames using in-situ particle sampling and differential mobility analysis verified with two-colour time-resolved laser-induced incandescence. *Proceedings of the Combustion Institute, 39*(1), 1119–1128. https://doi.org/10.1016/j.proci.2022.07.253

Halmer, D., von Basum, G., Hering, P., & Mürtz, M. (2004). Fast exponential fitting algorithm for real-time instrumental use. *Review of Scientific Instruments, 75*(6), 2187–2191. https://doi.org/10.1063/1.1711189

Haynes, B. S., & Wagner, H. G. (1981). Soot formation. *Progress in Energy and Combustion Science, 7*(4), 229–273. https://doi.org/10.1016/0360-1285(81)90001-0

Irimiea, C., Faccinetto, A., Carpentier, Y., Ortega, I.-K., Nuns, N., Therssen, E., Desgroux, P., & Focsa, C. (2018). A comprehensive protocol for chemical analysis of flame combustion emissions by secondary ion mass spectrometry. *Rapid Communications in Mass Spectrometry, 32*(13). https://doi.org/10.1002/rcm.8133. Article 13.

Johansson, K. O., El Gabaly, F., Schrader, P. E., Campbell, M. F., & Michelsen, H. A. (2017). Evolution of maturity levels of the particle surface and bulk during soot growth and oxidation in a flame. *Aerosol Science and Technology, 51*(12), 1333–1344. https://doi.org/10.1080/02786826.2017.1355047

Kholghy, M. R., Kelesidis, G. A., & Pratsinis, S. E. (2018). Reactive polycyclic aromatic hydrocarbon dimerization drives soot nucleation. *Physical Chemistry Chemical Physics, 20*(16), 10926–10938. https://doi.org/10.1039/C7CP07803J

Lemaire, R., & Menanteau, S. (2021). Modeling laser-induced incandescence of Diesel soot—implementation of an advanced parameterization procedure applied to a refined LII model accounting for shielding effect and multiple scattering within aggregates for alpha$_T$ and E(m) assessment. *Applied Physics B, 127*(10), 138. https://doi.org/10.1007/s00340-021-07665-y

Lemaire, R., & Menanteau, S. (2023). Study of the wavelength dependence of the absorption function of diesel soot by LII modeling integrating the effect of multiple scattering within aggregates. *Applied Physics B, 129*(5), 79. https://doi.org/10.1007/s00340-023-08002-1

Liu, C., Singh, A. V., Saggese, C., Tang, Q., Chen, D., Wan, K., Vinciguerra, M., Commodo, M., De Falco, G., Minutolo, P., D'Anna, A., & Wang, H. (2019). Flame-formed carbon nanoparticles exhibit quantum dot behaviors. *Proceedings of the National Academy of Sciences, 116*(26), 12692–12697. https://doi.org/10.1073/pnas.1900205116

Liu, F., Stagg, B. J., Snelling, D. R., & Smallwood, G. J. (2006). Effects of primary soot particle size distribution on the temperature of soot particles heated by a nanosecond pulsed laser in an atmospheric laminar diffusion flame. *International Journal of Heat and Mass Transfer, 49*(3), 777–788. https://doi.org/10.1016/j.ijheatmasstransfer.2005.07.041

Liu, F., Yon, J., Fuentes, A., Lobo, P., Smallwood, G. J., & Corbin, J. C. (2020). Review of recent literature on the light absorption properties of black carbon: Refractive index, mass absorption cross section, and absorption function. *Aerosol Science and Technology, 54*(1), 33–51. https://doi.org/10.1080/02786826.2019.1676878

López-Yglesias, X., Schrader, P. E., & Michelsen, H. A. (2014). Soot maturity and absorption cross sections. *Journal of Aerosol Science, 75*, 43–64. https://doi.org/10.1016/j.jaerosci.2014.04.011

Maffi, S., De Iuliis, S., Cignoli, F., & Zizak, G. (2011). Investigation on thermal accommodation coefficient and soot absorption function with two-color Tire-LII technique in rich premixed flames. *Applied Physics B, 104*(2), 357–366. https://doi.org/10.1007/s00340-011-4536-x

Mannazhi, M., Bergqvist, S., Török, S., Madsen, D., Tóth, P., Le, K. C., & Bengtsson, P.-E. (2023). Strongly reduced optical absorption efficiency of soot with addition of potassium chloride in sooting premixed flames. *Proceedings of the Combustion Institute, 39*(1), 867–876. https://doi.org/10.1016/j.proci.2022.07.143

Maricq, M. M., Harris, S. J., & Szente, J. J. (2003). Soot size distributions in rich premixed ethylene flames. *Combustion and Flame, 132*(3), 328–342. https://doi.org/10.1016/S0010-2180(02)00502-3

Martin, J. W., Salamanca, M., & Kraft, M. (2022). Soot inception: Carbonaceous nanoparticle formation in flames. *Progress in Energy and Combustion Science, 88*, Article 100956. https://doi.org/10.1016/j.pecs.2021.100956

Mercier, X., & Desgroux, P. (2009). Cavity ring-down spectroscopy for combustion studies. In *Cavity ring-down spectroscopy: Techniques and applications* (pp. 273–311). Wiley-Blackwell. https://doi.org/10.1002/9781444308259.ch10. Scopus.

Michelsen, H. A. (2017). Probing soot formation, chemical and physical evolution, and oxidation: A review of in situ diagnostic techniques and needs. *Proceedings of the Combustion Institute, 36*(1), 717–735. https://doi.org/10.1016/j.proci.2016.08.027

Michelsen, H. A. (2021). Effects of maturity and temperature on soot density and specific heat. *Proceedings of the Combustion Institute, 38*(1), 1197–1205. https://doi.org/10.1016/j.proci.2020.06.383

Michelsen, H. A., Colket, M. B., Bengtsson, P.-E., D'Anna, A., Desgroux, P., Haynes, B. S., Miller, J. H., Nathan, G. J., Pitsch, H., & Wang, H. (2020). A review of terminology used to describe soot formation and evolution under combustion and pyrolytic conditions. *ACS Nano, 14*(10). https://doi.org/10.1021/acsnano.0c06226. Article 10.

Migliorini, F., Iuliis, S. D., Cignoli, F., & Zizak, G. (2008). How "flat" is the rich premixed flame produced by your McKenna burner? *Combustion and Flame, 153*(3), 384–393. https://doi.org/10.1016/j.combustflame.2008.01.007

Migliorini, F., Thomson, K. A., & Smallwood, G. J. (2011). Investigation of optical properties of aging soot. *Applied Physics B, 104*(2), 273–283. https://doi.org/10.1007/s00340-011-4396-4

Minutolo, P., Commodo, M., & D'Anna, A. (2023). Optical properties of incipient soot. *Proceedings of the Combustion Institute, 39*(1), 1129–1138. https://doi.org/10.1016/j.proci.2022.09.019

Moallemi, A., Kazemimanesh, M., Kostiuk, L. W., & Olfert, J. S. (2018). The effect of sodium chloride on the nanoparticles observed in a laminar methane diffusion flame. *Combustion and Flame, 188*, 273–283. https://doi.org/10.1016/j.combustflame.2017.10.009

Mouton, T., Mercier, X., Wartel, M., Lamoureux, N., & Desgroux, P. (2013). Laser-induced incandescence technique to identify soot nucleation and very small particles in low-pressure methane flames. *Applied Physics B, 112*(3), 369–379. https://doi.org/10.1007/s00340-013-5446-x

Olofsson, N.-E., Simonsson, J., Török, S., Bladh, H., & Bengtsson, P.-E. (2015). Evolution of properties for aging soot in premixed flat flames studied by laser-induced incandescence and elastic light scattering. *Applied Physics B, 119*(4), 669–683. https://doi.org/10.1007/s00340-015-6067-3

Schenk, M., Lieb, S., Vieker, H., Beyer, A., Gölzhäuser, A., Wang, H., & Kohse-Höinghaus, K. (2015). Morphology of nascent soot in ethylene flames. *Proceedings of the Combustion Institute, 35*(2), 1879–1886. https://doi.org/10.1016/j.proci.2014.05.009

Schoemaecker Moreau, C., Therssen, E., Mercier, X., Pauwels, J. F., & Desgroux, P. (2004). Two-color laser-induced incandescence and cavity ring-down spectroscopy for sensitive and quantitative imaging of soot and PAHs in flames. *Applied Physics B, 78*(3), 485–492. https://doi.org/10.1007/s00340-003-1370-9

Sgro, L. A., Barone, A. C., Commodo, M., D'Alessio, A., Filippo, A. D., Lanzuolo, G., & Minutolo, P. (2009). Measurement of nanoparticles of organic carbon in non-sooting flame conditions. *Proceedings of the Combustion Institute, 32*(1), 689–696. https://doi.org/10.1016/j.proci.2008.06.216

Simonsson, J., Olofsson, N.-E., Török, S., Bengtsson, P.-E., & Bladh, H. (2015). Wavelength dependence of extinction in sooting flat premixed flames in the visible and near-infrared regimes. *Applied Physics B, 119*(4), 657–667. https://doi.org/10.1007/s00340-015-6079-z

Snelling, D. R., Liu, F., Smallwood, G. J., & Gülder, Ö. L. (2004). Determination of the soot absorption function and thermal accommodation coefficient using low-fluence LII in a laminar coflow ethylene diffusion flame. *Combustion and Flame, 136*(1), 180–190. https://doi.org/10.1016/j.combustflame.2003.09.013

Stirn, R., Baquet, T. G., Kanjarkar, S., Meier, W., Geigle, K. P., Grotheer, H. H., Wahl, C., & Aigner, M. (2009). Comparison of particle size measurements with laser-induced incandescence, mass spectroscopy, and scanning mobility particle sizing in a laminar premixed ethylene/air flame. *Combustion Science and Technology, 181*(2), 329–349. https://doi.org/10.1080/00102200802483498

Tang, Q., Cai, R., You, X., & Jiang, J. (2017). Nascent soot particle size distributions down to 1nm from a laminar premixed burner-stabilized stagnation ethylene flame. *Proceedings of the Combustion Institute, 36*(1), 993–1000. https://doi.org/10.1016/j.proci.2016.08.085

Therssen, E., Bouvier, Y., Schoemaecker-Moreau, C., Mercier, X., Desgroux, P., Ziskind, M., & Focsa, C. (2007). Determination of the ratio of soot refractive index function E(m) at the two wavelengths 532 and 1064 nm by laser induced incandescence. *Applied Physics B, 89*(2), 417–427. https://doi.org/10.1007/s00340-007-2759-7

Thomson, M. J. (2023). Modeling soot formation in flames and reactors: Recent progress and current challenges. *Proceedings of the Combustion Institute, 39*(1), 805–823. https://doi.org/10.1016/j.proci.2022.07.263

Tian, K., Liu, F., Thomson, K. A., Snelling, D. R., Smallwood, G. J., & Wang, D. (2004). Distribution of the number of primary particles of soot aggregates in a nonpremixed laminar flame. *Combustion and Flame, 138*(1). https://doi.org/10.1016/j.combustflame.2004.04.008. Article 1.

Vander Wal, R. L., & Ticich, T. M. (1999). Cavity ringdown and laser-induced incandescence measurements of soot. *Applied Optics, 38*(9), 1444–1451. https://doi.org/10.1364/AO.38.001444

Wan, K., Shi, X., & Wang, H. (2021). Quantum confinement and size resolved modeling of electronic and optical properties of small soot particles. *Proceedings of the Combustion Institute, 38*(1), 1517–1524. https://doi.org/10.1016/j.proci.2020.07.145

Wang, H. (2011). Formation of nascent soot and other condensed-phase materials in flames. *Proceedings of the Combustion Institute, 33*(1), 41–67. https://doi.org/10.1016/j.proci.2010.09.009

Williams, T. C., Shaddix, C. R., Jensen, K. A., & Suo-Anttila, J. M. (2007). Measurement of the dimensionless extinction coefficient of soot within laminar diffusion flames. *International Journal of Heat and Mass Transfer, 50*(7), 1616–1630. https://doi.org/10.1016/j.ijheatmasstransfer.2006.08.024

Yon, J., Lemaire, R., Therssen, E., Desgroux, P., Coppalle, A., & Ren, K. F. (2011). Examination of wavelength dependent soot optical properties of diesel and diesel/rapeseed methyl ester mixture by extinction spectra analysis and LII measurements. *Applied Physics B, 104*(2), 253–271. https://doi.org/10.1007/s00340-011-4416-4

Zerbs, J., Geigle, K. P., Lammel, O., Hader, J., Stirn, R., Hadef, R., & Meier, W. (2009). The influence of wavelength in extinction measurements and beam steering in laser-induced incandescence measurements in sooting flames. *Applied Physics B, 96*(4). https://doi.org/10.1007/s00340-009-3550-8. Article 4.

Zhao, B., Uchikawa, K., & Wang, H. (2007). A comparative study of nanoparticles in premixed flames by scanning mobility particle sizer, small angle neutron scattering, and transmission electron microscopy. *Proceedings of the Combustion Institute, 31*(1), 851–860. https://doi.org/10.1016/j.proci.2006.08.064